

A Fast Frequency-Domain Algorithm for Gravitational Self-Force: Circular Orbits in Schwarzschild Spacetime

Sarp Akcay

*School of Mathematics, University of Southampton, Southampton, SO17 1BJ, United Kingdom.**

Fast, reliable orbital evolutions of compact objects around massive black holes will be needed as input for gravitational wave search algorithms in the data stream generated by the planned Laser Interferometer Space Antenna (LISA). Currently, the state of the art is a time-domain code by [Phys. Rev. D **81**, 084021, (2010)] that computes the gravitational self-force on a point-particle in an eccentric orbit around a Schwarzschild black hole. Existing time-domain codes take up to a few days to compute just one point in parameter space. In a series of articles, we advocate the use of a frequency-domain approach to the problem of gravitational self-force (GSF) with the ultimate goal of orbital evolution in mind. Here, we compute the GSF for a particle in a circular orbit in Schwarzschild spacetime. We solve the linearized Einstein equations for the metric perturbation in Lorenz gauge. Our frequency-domain code reproduces the time-domain results for the GSF up to ~ 1000 times faster for small orbital radii. In forthcoming companion papers, we will generalize our frequency-domain computations of the GSF to include bound (eccentric) orbits in Schwarzschild spacetimes, where we will employ the method of extended homogeneous solutions [Phys. Rev. D **78**, 084021 (2008)]. We will eventually extend our methods to attempt a frequency-domain computation of the GSF in Kerr spacetime.

I. INTRODUCTION

With the start of the upgrades to second generation ground based gravitational wave detectors [3, 4] and the approval of the LISA Pathfinder mission [5], the age of gravitational wave (GW) astronomy has begun. One promising source of gravitational radiation is the so-called extreme mass ratio inspirals (EMRIs) where a compact object (a black hole or a neutron star) of a few solar masses slowly spirals in toward a massive black hole (MBH). The compact object (CO) interacts with its own gravitational field, which causes it to move on a path perturbed from the geodesic of the background spacetime. Along this ‘forced’ trajectory, the object radiates gravitationally losing energy and angular momentum. For CO to MBH mass ratios of $\sim 10^{-5} - 10^{-6}$, the frequency of the gravitational waves emitted during the last few years of inspiral (up to the final plunge) will be a few mHz, which will fall right in the middle of LISA’s frequency band [6]. Analysis of the waveforms emanating from these inspirals will provide us with an unprecedented way of mapping spacetime around the central objects [7], which are presumed to be Kerr black holes. A typical LISA bandwidth EMRI will be a $\sim 1.5M_{\odot}$ neutron star/black hole inspiraling onto a $\sim 10^6M_{\odot}$ MBH. In its last year before the plunge, the compact object will spiral in from a distance of $\sim 10GM/c^2$ to the innermost stable circular orbit ($6GM/c^2$ for Schwarzschild black hole) executing $\sim 5 \times 10^4$ orbits and sweeping the GW frequency band from ~ 2 mHz to ~ 5 mHz [8]. Such sources will be detectable by LISA for years, but the amplitude of the resulting gravitational wave strain will be smaller than the noise in the instrument [9]. However, matched-filtering the signal over an extended period of time (\sim few years) will bump the signal-to-noise ratio as high as 100 for the nearest sources [10]. To be able to use matched-filtering, very accurate gravitational wave templates will be required as input for the cross-correlation. This will call for very accurate simulations of these inspirals over their LISA bandwidth lifetimes. The most challenging part in obtaining reliable simulations will be keeping track of the orbital phase as over the course of the inspiral the accumulated phase error should not exceed a few radians out of a total of $\mathcal{O}(10^5) - \mathcal{O}(10^6)$ radians. This will put quite a stringent limit on the error tolerance of orbital evolution models.

This is where the gravitational self-force comes in. In the test mass ($\mu = 0$) case, the CO follows a geodesic of the background spacetime. However, for a small, but finite mass the CO (modelled as a point particle sourced by a Dirac delta function) interacts with its own gravitational field, which scatters off the curvature of the background spacetime. This interaction can be interpreted as perturbing the particle’s path off the background geodesic. In other words, the particle now accelerates, thus feels a net force due to this back-reaction. This is what has become known as the gravitational self-force (GSF).

The study of radiation reaction began not with the GSF but with electromagnetic self-force (SF). This problem was first successfully worked out by DeWitt & Brehme [11]. Later, the solution to the gravitational problem was

*Electronic address: sa18g09@soton.ac.uk

formulated by Mino, Sasaki & Tanaka [12] and independently by Quinn & Wald [13] in terms of “forced geodesics” where the compact object feels a net force and is pushed off the geodesic of the unperturbed background spacetime. This approach is generally known as the MiSaTaQuWa formulation. Detweiler & Whiting [14] provided an alternate formulation based on geodesics of a perturbed spacetime. These were followed by [15–19], which developed more practical methods for computing the actual self-force in Schwarzschild and Kerr spacetimes. They employed the so-called “mode-sum scheme” in which the scalar, vector or the tensor perturbation is decomposed in terms of corresponding spherical harmonics. In the case of GSF, a tensor spherical harmonic decomposition of the retarded metric perturbation $\bar{h}_{\mu\nu}(t, \mathbf{x})$ is performed. Then, the resulting 10 second order coupled partial differential equations are solved numerically at each tensor mode (ℓ, m) . The resulting metric fields and their derivatives are added together in certain combinations. These combinations are then translated from tensor modes to scalar (l, m) modes to yield individual l modes of the ‘full’ GSF given by Eq.(72). As the full GSF is singular at the location of the particle, a regularization procedure is undertaken. In MiSaTaQuWa formulation, this is done by decomposing the divergent ‘direct’ part of the GSF into scalar spherical harmonics then removing these from the full GSF at each l mode. The resulting regularized l modes are finite and yield a convergent sum. This sidesteps the issue of dealing with infinities. The final GSF is then given by summing over the l modes from zero to infinity.

The mode-sum scheme has thus far been implemented by several groups for SF computations [21] - [31]. Most of these have been for scalar field SF or looked at simplified cases for GSF computations (in Schwarzschild) such as radial infall or a static particle. The GSF for circular orbits in Schwarzschild was first successfully calculated (in time domain) by Barack & Sago [32]. This was soon-after followed by independent calculations by Detweiler [34] and Berndtson [35]. Although these calculations used different gauges and methods, by comparing the effects of the GSF on gauge invariant quantities derived by Detweiler [34], these three independent GSF computations were shown to be equivalent [35, 36]. The state of the art for GSF computations is the recent work of Barack & Sago on eccentric orbits in Schwarzschild spacetime [1]. Some progress has also been made for GSF computations in Kerr spacetime, the state of the art being the work of Warburton & Barack [38] on scalar field SF for bound (eccentric, equatorial) orbits in Kerr spacetime. This work was successfully implemented in frequency domain using the recently developed method of extended homogeneous solutions [39]. This was a very important step in the efforts to compute the GSF using frequency-domain methods. The method of extended homogeneous solutions successfully avoids the ‘Gibbs phenomenon’ that causes the radial derivatives of the metric fields to be averaged out across the point particle as opposed to displaying the expected finite jump there, which is the result of modeling the particle as a delta-function distribution. A very thorough introduction to the fundamentals of the self-force problem is presented by Poisson [40]. In addition, a recent article by Barack [41] overviews the current state of the field.

Our aim in this part I of the series is to provide a fast framework for computing the GSF that can be used for orbital evolutions. For this reason, we have chosen to work in frequency domain (f-domain). Berndtson [35] was the first to successfully compute the GSF for circular orbits in Schwarzschild using f-domain methods, but his method differs from ours and his work is unpublished. Starting with Regge & Wheeler’s (RW) standard tensor harmonic decomposition of the metric perturbation [42], Berndtson solved the field equations in Lorenz gauge by relating the gauge invariant RW, Zerilli master functions [43] to the unknown metric fields of Lorenz gauge. It turned out, however, that he did not have the correct expression for the contribution of the monopole mode to the GSF. But when he adopted Detweiler & Poisson’s [33] solution for this mode, the results he obtained for the GSF matched those of [32]. His results also highlighted the key advantages of a f-domain computation, namely, higher accuracy and faster runtimes compared to time-domain methods.

Despite the evident success of Berndtson’s approach, it is our feeling that our f-domain approach is better suited for extension to Kerr in that it relies less on the spherical symmetry of the background spacetime. As there currently exist no tensor spheroidal harmonics, we must rely on a tensor spherical harmonic decomposition of the metric perturbation in Kerr. The problem then is that the resulting ordinary differential equations (ODEs) couple between different multiple modes, not just metric fields. However, the principal parts of the ODEs remain uncoupled and it is possible to numerically solve the resulting system of coupled ODEs by treating the extra couplings as new source terms. We refrain from elaborating further as this problem is beyond the scope of this article but our longterm research program includes tackling these issues.

The obvious advantage of working in the f-domain is that one deals only with ODEs, which can be solved efficiently using numerical methods. Furthermore, in f-domain, there are no instabilities associated with the non-radiative modes (monopole, dipole) that one encounters in the time domain [30, 32]. However, there are downsides to working in the f-domain. One is that f-domain methods work only for bound orbits. Also, it is generally thought that f-domain computations of GSF are intractable beyond eccentricities of approximately 0.7 [44]. The breakdown of f-domain computations is caused by the fact that as the eccentricity increases, there are more and more radial frequency modes per given azimuthal mode. This significantly augments the runtimes of numerical computations. Eventually, one expects to reach a threshold eccentricity at which the use of time-domain methods becomes numerically more efficient. It is likely that f-domain methods become computationally inefficient (compared to time-domain) at eccentricities

higher than 0.7. We hope to empirically determine this threshold value in our future work. However, this may not necessarily present a problem since EMRI orbits circularize [45] as they shrink toward the last stable orbit and despite recent findings [9], [10] that we should expect to see EMRIs with moderate eccentricities in the LISA bandwidth, most of the eccentricity will have been reduced by the time the compact object begins its final year of inspiral so that there should be plenty of EMRIs with eccentricities $\lesssim 0.2$ for LISA to detect. For such eccentricities, we expect an f-domain code to be significantly faster than its time-domain counterparts.

As the GSF is a gauge dependent quantity (as is the orbital radius), we must address the issue of gauge choice used in our GSF computations. Lorenz gauge is a common choice in perturbative studies of curved spacetimes at linear order. One is motivated by this gauge choice because it retains the local isotropy of the delta-function singularity used to model the compact object [46]. It also casts the field equations in a fully hyperbolic form, which is suitable for time-domain calculations. On the other hand, the perturbed field equations are generally more tractable in gauges like the Regge-Wheeler (RW) [42] or the radiation gauges [47]. However, thanks to the work of Barack & Lousto [20], we now have access to all of the field equations in Lorenz gauge and can follow an “all-Lorenz-gauge” path. This is especially desirable in the mode-sum scheme because the multipole modes of the metric perturbation ($\bar{h}_{\mu\nu}^{\ell m}(t, r)$) in Lorenz gauge are continuous (C^0) at the location of the particle. This is not the case, for example, in RW gauge where the source contains a derivative-of-delta-function term in addition to the usual delta function. Therefore, the so-called “master functions” used in the RW formalism exhibit a jump-discontinuity (C^{-1}) at the location of the compact object. Finally, one can compute only the radiative ($\ell \geq 2$) modes of the perturbation using approaches based on RW gauge [48].

Our treatment here is mostly based on the work of Barack & Lousto [20] (henceforth BL) and Barack & Sago 2007 [32] (BS), which use the mode-sum method in Lorenz gauge. We begin with the linearized Einstein equations in Schwarzschild background in Lorenz gauge. We then rewrite the field equations using tensor spherical harmonic decomposition of the metric perturbations. This decouples the angular part of the field equations. The resulting set of 10 second order partial differential equations are separated into 7 even and 3 odd parity equations. Next, we go into the frequency domain and obtain $7 \oplus 3$ second order ODEs. For a generic bound orbit, we would need to sum over radial and azimuthal frequency modes to work in f-domain, but for circular orbits we have only one fundamental (azimuthal) frequency. Therefore, the crucial step in moving to an f-domain computation for circular orbits is supplying appropriate boundary conditions for the metric fields. Here, we present these boundary conditions (BC) for the first time.

With the BC specified, we numerically solve the coupled homogeneous ODEs then impose junction conditions at the location of the particle to construct the inhomogeneous solutions. Once we construct all the metric perturbations and their derivatives at the particle, we compute the GSF by using the formulae derived in BS. This gives us what is called the “full self-force”. It contains a ‘tail’ contribution, which we interpret as the relevant physical piece and a ‘direct’ part, which must be removed via the appropriate regularization procedure. It should be iterated that the initial decomposition of the metric perturbation is done in *tensor* spherical harmonics, whereas the regularization is performed using *scalar* spherical harmonics. This requires us to translate each tensor (ℓ, m) mode to various scalar (l, m) modes before regularizing. This causes a single scalar mode l to couple to many tensor modes ℓ . The formulae for these couplings have been derived by BS. Here, we use their results to compute the GSF.

For circular orbits, only the r -component of the GSF needs be regularized. In the mode-sum scheme, this is done mode-by-mode at each scalar multipole l where the singular piece is decomposed in *scalar* spherical harmonics then is removed from the full self-force at each l . The resulting regularized l modes have l^{-2} large- l behavior, which yields a convergent (albeit somewhat slow) sum over l . The physical self-force is obtained by summing over all the individual regularized l modes and finally adding a large- l “tail” that estimates the total contribution due to $l > l_{max}$ modes where l_{max} is the largest mode at which we actually compute the metric perturbations.

Section II presents the field equations and their decomposition under tensor spherical harmonics. In section III, we go into f-domain by Fourier transforming the time dependence of the metric fields in azimuthal frequency modes. We then separate the resulting field equations under their parity and calculate the BC for each case separately. Once the BC are known, the numerical ODE solver integrates the field equations to yield the homogeneous solutions. Using these, we assemble the inhomogeneous solutions, which we use in section IV to construct the full GSF, which we then regularize. Finally, we compute the tail contribution to the r -component of the GSF. The results are all displayed in section V where we compare the t, r -components of the GSF computed by our code with that of BS. We find an excellent agreement with BS within their error bars for orbital radii up to $\sim 100GM/c^2$.

Throughout this article, we use geometrized units with $G = c = 1$. $x^\mu = (t, r, \theta, \phi)$ are the standard Schwarzschild coordinates and τ denotes proper time. We follow the usual convention of $(-, +, +, +)$ for the metric signature. Finally, owing to the spherical symmetry of Schwarzschild spacetime, we work with equatorial $\theta = \pi/2$ orbits without loss of generality.

II. FIELD EQUATIONS

The physical set-up is that of a point particle with mass μ in a circular orbit with radius r_0 around a Schwarzschild black hole with mass M . The particle interacts with its own gravitational field and thus feels a net force which moves it off the geodesics of the background spacetime. The equation of motion for the particle in this context is given by

$$\mu u^\mu \nabla_\mu u^\nu = F_{\text{GSF}}^\nu, \quad (1)$$

where $u^\mu \equiv dx^\mu/d\tau$ denotes the 4-velocity of the particle, τ is proper time, ∇_μ is the covariant gradient operator associated with the background Schwarzschild metric and F_{GSF}^μ is the gravitational SF. Imposing the condition that the 4-velocity remain normalized along the worldline i.e. $u_\mu u^\mu = -1$ on Eq. (1), we get the orthogonality condition on the self-force: $u_\mu F_{\text{GSF}}^\mu = 0$. For circular orbits, $F_{\text{GSF}}^t, F_{\text{GSF}}^\phi$ can be calculated independently using energy balance arguments [49] because they are purely dissipative. However, in the case of eccentric orbits all non-zero components of the SF will be made up of both dissipative and conservative parts. The orthogonality condition is useful because it gives us a simple way to obtain one out of the three components of the GSF (fourth component $F_{\text{GSF}}^\theta = 0$ because of spherical symmetry).

To obtain the GSF in this ‘‘forced geodesic’’ picture, we must solve the perturbed Einstein’s equation in a non-flat background. Schematically, the field equations have the following form

$$G_{\mu\nu}[\mathring{g}_{\mu\nu} + h_{\mu\nu}] = 8\pi T_{\mu\nu}, \quad (2)$$

where $G_{\mu\nu}$ is the Einstein tensor, which is a functional of the spacetime metric $g_{\mu\nu} = \mathring{g}_{\mu\nu} + h_{\mu\nu}$ and $T_{\mu\nu}$ is the energy-momentum tensor sourced by the point particle. Here, $\mathring{g}_{\mu\nu}$ denotes the background (vacuum) Schwarzschild metric and $h_{\mu\nu}$ is the perturbation due to the point particle. As is standard with current GSF computations, we retain only the linear order $\mathcal{O}(\mu)$ perturbation. There are ongoing efforts to incorporate second order perturbations in the calculations of GSF [50, 51], but the current formulations are not yet ready for use in mode-sum GSF computations.

After keeping up to $\mathcal{O}(h_{\mu\nu})$ terms in Eq.(2), we substitute $G[\mathring{g}] = 0$ into Eq.(2) since $\mathring{g}_{\mu\nu}$ is the metric of a vacuum spacetime. We make two more simplifications, which are standard: first, we change from using $h_{\mu\nu}$ to the trace-reversed $\bar{h}_{\mu\nu}$ via $\bar{h}_{\mu\nu} = h_{\mu\nu} - \frac{1}{2}g_{\mu\nu}h$. Then, we pick a gauge. For reasons explained above and detailed in the cited articles, we choose to work in Lorenz gauge where $\nabla_\mu \bar{h}^{\mu\nu} = 0$. With these modifications inserted into Eq. (2) we obtain

$$\square \bar{h}_{\mu\nu} + 2\mathring{R}^{\alpha\beta} \bar{h}_{\alpha\beta} = -16\pi T_{\mu\nu}, \quad (3)$$

where $\square = \nabla_\mu \nabla^\mu$. The energy-momentum tensor is given by

$$T_{\mu\nu} = \mu \int_{-\infty}^{\infty} (-\mathring{g})^{-1/2} \delta^4[x^\mu - x_0^\mu(\tau)] u_\mu u_\nu d\tau, \quad (4)$$

where $x^\mu(\tau)$ denotes the position of the particle. The proper time τ is related to the coordinate time t via $d\tau = (u^t)^{-1} dt$. Finally, \mathring{g} is the determinant of the Schwarzschild metric equaling $-r_0^4$ for $\theta = \pi/2$.

As it stands, Eq. (3) represents 10 coupled 2nd order, partial differential equations (PDEs). We can simplify these by separating out the angular part. To this end, we decompose $\bar{h}_{\mu\nu}(t, \mathbf{r})$ using *tensor* spherical harmonics, which form a 10-dimensional basis for any rank two, symmetric 4-dimensional tensor field. The components of the metric perturbation are decomposed as follows:

$$\bar{h}_{\mu\nu}(t, \mathbf{r}) = \frac{\mu}{r} \sum_{\ell, m} \sum_{i=1}^{10} \bar{h}^{(i)\ell m}(t, r) Y_{\mu\nu}^{(i)\ell m}(\theta, \phi; r). \quad (5)$$

The explicit expressions for $Y_{\mu\nu}^{(i)\ell m}$ are presented in BL. We modify them slightly here: $Y_{\mu\nu}^{(i)\ell m} \text{ here} = a^{(i)\ell} Y_{\mu\nu}^{(i)\ell m} \text{ BL}$ where $a^{(i)\ell}$ constant coefficients defined in BL. Now angular variables decouple and the field equations become (at each ℓ, m)

$$\square_{sc} \bar{h}^{(i)\ell m} + \mathcal{M}_{(j)}^{(i)} \bar{h}^{(j)\ell m} = \mathcal{S}^{(i)\ell m}. \quad (6)$$

where $f = f(r) \equiv 1 - \frac{2M}{r}$ and \square_{sc} is the usual scalar field wave operator:

$$\square_{sc} = \frac{1}{4} \left[\partial_t^2 - \partial_{r^*}^2 + f \left(\frac{2M}{r^3} + \frac{\ell(\ell+1)}{r^2} \right) \right]. \quad (7)$$

$\mathcal{S}^{(i)}$ are the source terms obtained from decomposing $T_{\mu\nu}$ in tensor spherical harmonics. They are given by

$$\mathcal{S}^{(i)\ell m} = 4\pi\tilde{E}_0 \alpha^{(i)} \times \delta(r - r_0) \begin{cases} [Y^{\ell m}(\theta, \Omega_0 t)]^* & i = 1, 2, \dots, 7 \\ \partial_\theta [Y^{\ell m}(\theta, \Omega_0 t)]^* & i = 8, 9, 10 \end{cases} \quad (8)$$

where $\tilde{E}_0 = (1 - 2M/r_0)/\sqrt{1 - 3M/r_0}$ is the dimensionless energy of a test particle ($\mu = 0$) on a circular geodesic with radius r_0 . Given the orbital angular frequency $\Omega_0 = d\phi_0/dt = (M/r_0^3)^{1/2}$, the constants $\alpha^{(i)}$ are:

$$\begin{aligned} \alpha^{(1)} &= f_0^2/r_0, & \alpha^{(3)} &= f_0/r_0, & \alpha^{(7)} &= r_0\Omega_0^2[\ell(\ell+1) - 2m^2], \\ \alpha^{(2),(5),(9)} &= 0, & \alpha^{(8)} &= 2f_0\Omega_0, \\ \alpha^{(4)} &= 2if_0m\Omega_0, & \alpha^{(10)} &= 2imr_0\Omega_0^2, \\ \alpha^{(6)} &= r_0\Omega_0^2, \end{aligned} \quad (9)$$

where $f_0 = 1 - 2M/r_0$. Note that the $(i) = 2, 5, 9$ equations are sourceless. The spherical harmonics are given by the usual formula

$$Y^{\ell m}(\theta, \phi) = \hat{c}_{\ell m} P^{\ell m}(\theta) e^{im\phi}. \quad (10)$$

$P^{\ell m}(\theta)$ are the associated Legendre polynomials and $\hat{c}_{\ell m} \equiv \sqrt{\frac{2\ell+1}{4\pi} \frac{(\ell-m)!}{(\ell+m)!}}$. We can further rewrite the second line in Eq. (8) using the following expression:

$$\begin{aligned} \partial_\theta [Y^{\ell m}(\pi/2, \phi_0)]^* &= [\ell C_{\ell+1,m} \hat{c}_{\ell+1,m} P^{\ell+1,m}(\pi/2) - (\ell+1) C_{\ell m} \hat{c}_{\ell m} P^{\ell-1,m}(\pi/2)] e^{-im\phi_0} \\ &\equiv \mathcal{J}_{\ell m}^{(\text{odd})} e^{-im\phi_0} \end{aligned} \quad (11)$$

where $C_{\ell m} = \sqrt{\frac{\ell^2 - m^2}{(2\ell+1)(2\ell-1)}}$.

The $\mathcal{M}_{(j)}^{(i)} \bar{h}^{(j)}$ in Eq. (6) contain the coupling terms between different field equations. In the next section, we will show that up to 5 field equations couple together for certain modes, but things will not get any more entwined than that. The expressions for $\mathcal{M}_{(j)}^{(i)} \bar{h}^{(j)}$ are lengthy and have been given in detail in [1], [20] and [32] so we omit them here. We will however present the field equations in frequency domain in section III.

Eq. (8) substituted in to Eq. (6) gives us the Einstein field equations in their simplest form that we can reach in Lorenz gauge. From this point, one can either go into time domain and tackle the problem of solving these coupled PDEs or one can go into frequency domain and deal with ODEs that require boundary conditions. In the next section, we solve the field equations in frequency domain in Lorenz gauge for the first time.

III. FREQUENCY-DOMAIN SOLUTIONS OF THE FIELD EQUATIONS

Here, we begin by decomposing the metric fields $\bar{h}^{(i)}(t, r)$ into frequency modes. In the case of circular orbits, there is only one frequency: $\Omega_0 = (M/r_0^3)^{1/2}$. So the harmonics of circular motion are given by $\omega_m = m\Omega_0$. For elliptical orbits, the frequency modes will be a combination of azimuthal and radial fundamental frequencies: $\omega_{mn} = m\Omega_\phi + n\Omega_r$. For circular orbits, metric fields are decomposed as follows:

$$\bar{h}^{(i)\ell m}(t, r) = R_{\ell m}^{(i)}(r) e^{-i\omega_m t}, \quad \text{where } \omega_m = m\Omega_0. \quad (12)$$

This reduces the 2-dimensional hyperbolic equations (6) to a set of 2nd order, coupled ODEs, which can be numerically solved much more quickly than PDEs encountered in time-domain approaches. In the case of a scalar field in Schwarzschild spacetime, the problem in f-domain reduces to a single inhomogeneous ODE. The standard procedure is to numerically solve for the *homogeneous* inner ($r < r_0$) and outer ($r > r_0$) solutions then construct the inhomogeneous solution by imposing the correct junction conditions at $r = r_0$. For the computation of the GSF, the same procedure applies but now for many coupled fields, some of which have delta-function sources and others no sources at all. In section III A 1, we explicitly show how we construct the inhomogeneous solutions from coupled homogeneous solutions.

The system of 10 coupled, second order homogeneous ODEs can be written as

$$\frac{d^2 R_{\ell m}^{(i)}(r)}{dr_*^2} - 4V_{\ell m}(r) R_{\ell m}^{(i)}(r) - 4\tilde{\mathcal{M}}_{(j)}^{(i)} R_{\ell m}^{(j)}(r) = 0. \quad (13)$$

where r_* is the Regge-Wheeler tortoise coordinate with $dr_*/dr = f^{-1}$, $\tilde{\mathcal{M}}_{(j)}^{(i)}$ is the Fourier transformed version of $\mathcal{M}_{(j)}^{(i)}$, and

$$V_{\ell m}(r) = \frac{1}{4} \left[\frac{2Mf}{r^3} + \frac{\ell(\ell+1)f}{r^2} - \omega_m^2 \right]. \quad (14)$$

The field equations (13) are not all coupled to each other; our 10-dimensional basis splits under parity very much like in Regge-Wheeler gauge. The $(i) = 1, \dots, 7$ basis elements of the tensor spherical harmonics are *even* and the $(i) = 8, 9, 10$ basis elements are *odd* under parity transformations. For circular orbits, *even*, *odd* mean that $\ell + m = \text{even}$, odd . Eqs. (13) now decouple completely under these two parity sectors so they can be solved completely independently. Furthermore, because the spherical harmonics in the source terms (8) give $[Y^{\ell m}(\pi/2, \phi_0)]^* = 0$ for $\ell + m = \text{odd}$ and $\partial_\theta [Y^{\ell m}(\pi/2, \phi_0)]^* = 0$ for $\ell + m = \text{even}$, the odd parity solutions are trivially zero for an even mode and vice versa for even parity solutions. That is $R^{(1)\dots(7)} = 0$ for $\ell + m = \text{odd}$ and $R^{(8),(9),(10)} = 0$ for $\ell + m = \text{even}$.

Similarly, the four gauge equations coming from the Lorenz gauge condition $\nabla_\mu \bar{h}^\mu_\nu = 0$ also decouple under parity with three equations falling under the even parity sector, leaving only one for the odd sector. The gauge equations at each (ℓ, m) -mode are

$$i\omega_m R^{(1)} + f \left(i\omega_m R^{(3)} + R_{,r}^{(2)} + \frac{R^{(2)}}{r} - \frac{R^{(4)}}{r} \right) = 0, \quad (15)$$

$$-i\omega_m R^{(2)} - f R_{,r}^{(1)} + f^2 R_{,r}^{(3)} - \frac{f}{r} \left(R^{(1)} - R^{(5)} - f R^{(3)} - 2f R^{(6)} \right) = 0, \quad (16)$$

$$-i\omega_m R^{(4)} - \frac{f}{r} \left(r R_{,r}^{(5)} + 2R^{(5)} + \ell(\ell+1)R^{(6)} - R^{(7)} \right) = 0, \quad (17)$$

$$-i\omega_m R^{(8)} - \frac{f}{r} \left(r R_{,r}^{(9)} + 2R^{(9)} - R^{(10)} \right) = 0. \quad (18)$$

Here and henceforth, we omit writing the modal indices ℓ, m as well as the functional dependence on r_* (or r) for the sake of brevity. It should be assumed that each field equation presented holds for a given ℓ, m mode unless stated otherwise.

Thanks to the gauge equations, it turns out that not all the even (or odd) equations need to be solved simultaneously. As we have four gauge conditions, we have only $10 - 4 = 6$ degrees of freedom (d.o.f). These split as $4 + 2$ under parity. But because of the particular form of the field equations in the even sector, we must solve 5 coupled ODEs together, construct the inhomogeneous solutions then use two gauge equations to obtain the fields $R^{(2)}$ and $R^{(4)}$ (more on this later in section III B). In the odd sector, we solve the two coupled $(i) = 9, 10$ equations together then use the odd gauge equation to obtain $R^{(8)}$. This procedure of solving the equations in stages is called “the hierarchical solving scheme” by BL. It involves first numerically solving only the ODEs that couple to each other then using gauge equations (15) - (18) to determine the remaining unknown radial fields. The number of equations one has to solve changes depending on the values of ℓ and m . For a generic even mode ($\ell \geq 2, m > 1$), one solves 5 coupled ODEs then uses two gauge equations whereas for a generic odd mode ($\ell \geq 2, m \geq 1$), only two coupled ODEs are solved numerically then one gauge equation is used. There are also non-generic modes such as the monopole ($\ell = 0$); the even, odd dipoles ($\ell = 1, m = 1, 0$) and the static ($m = 0$) even, odd modes. Analytic solutions have been explicitly provided in [33] for the monopole, and by BL for the odd static modes. The even dipole ($\ell = 1, m = 1$) and the $\ell = \text{even}$ static modes are solved numerically, but have fewer number of non-zero fields. We present all the different cases for both even and odd parity sectors and the hierarchical scheme for solving the field equations in table I

A. Odd Sector

We begin with what we call *generic* odd modes ($m > 0$). We will consider the static odd modes ($m = 0$) later in a special subsection. As explained in the hierarchical scheme, here we solve the coupled $(i) = 9, 10$ equations

	Even ($\ell + m = 2N$)	Odd ($\ell + m = 2N + 1$)
$\ell = 0$	$(i) = 1, 3, 6 \rightarrow 2$ (A)	no field
$\ell = 1$	$m = 1 : (i) = 1, 3, 5, 6 \rightarrow 2, 4$	$m = 0 : (i) = 8$ only (A)
$\ell \geq 2$	$(i) = 1, 3, 5, 6, 7 \rightarrow 2, 4$	$(i) = 9, 10 \rightarrow 8$
	$m = 0 : (i) = 1, 3, 5 \rightarrow 6, 7$	$m = 0 : (i) = 8$ only (A)

TABLE I: The hierarchical solving scheme for the ten field equations. The arrows \rightarrow indicate that we use the gauge equations to obtain the field to the right of the arrow. (A) indicates that the solutions are obtained analytically and $N \in \mathbb{N}$

together to determine $R^{(9)}$ and $R^{(10)}$ then use these solutions in the odd gauge equation (18) to solve for $R^{(8)}$. The two homogeneous, odd parity field equations are

$$\partial_{r_*}^2 R^{(9)} = 4 \left[V_{\ell m} + \frac{f}{r^2} \left(1 - \frac{4.5M}{r} \right) \right] R^{(9)} - \frac{2f}{r^2} \left(1 - \frac{3M}{r} \right) R^{(10)}, \quad (19)$$

$$\partial_{r_*}^2 R^{(10)} = 4 \left(V_{\ell m} - \frac{f}{2r^2} \right) R^{(10)} - \frac{2f\lambda}{r^2} R^{(9)}, \quad (20)$$

where $\lambda = (\ell + 2)(\ell - 1)$. In order to get the correct numerical solutions to Eqs. (19) and (20), we must specify appropriate boundary conditions for the numerical ODE integrator. The boundaries are located on the event horizon ($r = 2M$) and at radial infinity ($r = \infty$), which translate to $r_* = -\infty$ and $r_* = \infty$, respectively. A quick inspection of the structure of the ODEs ($i) = 9, 10$ reveals that as $r, r_* \rightarrow \infty$ and $r \rightarrow 2M$ ($r_* \rightarrow -\infty$), the ω_m^2 term dominates in the potential and the ODEs (19) and (20) asymptotically turn into standard wave equations. Thus, for the solutions at infinity and on the event horizon, we have the usual outgoing and ingoing wave behavior, respectively. Denoting the outgoing/ingoing *homogeneous* solutions by R_i^+ and R_i^- , respectively, we write the following ansatz for the boundary conditions:

$$R_{9,10}^+ = e^{i\omega_m r_*} \sum_{k=0}^{\infty} \frac{a_{9,10}^k}{r^k}, \quad (21)$$

$$R_{9,10}^- = e^{-i\omega_m r_*} \sum_{k=0}^{\infty} b_{9,10}^k (r - 2M)^k. \quad (22)$$

Clearly at $r = 2M$ and $r = \infty$ we get the proper wave-like behavior. We must also specify dR_i^\pm/dr ($i = 9, 10$) at the boundary points. Our numerical code uses r_* as the integration variable so we actually need $dR_i^\pm/dr_* = f dR_i^\pm/dr$ for the BC.

Numerically, we can not use infinities for the boundary points. For our code, we pick a range of $r_* \in [-65M, -55M]$ for the inner boundary. $r_* = -65M$, which corresponds to $r/M \approx (2 + 10^{-14})$ is about as far ‘in’ as we can go due to double floating point machine accuracy. The choice for the outer boundary point r_{out} depends on ℓ and ω_m as we demand that the outer boundary be located in the wave zone, which translates to $r_{\text{out}} \gg (\ell r_0)/\omega_m$. So we opt for an adaptive outer boundary at each (ℓ, m) where $r_{\text{out}} = 50 (\ell r_0)/\omega_m$. The ratio of 50 was chosen after numerical experimentation. Larger ratios mean larger runtimes for the computation of the homogeneous fields, and smaller ratios call for more terms in the series in Eqs.(21), (22) for numerical convergence.

Note that the sums for the BC in Eqs.(21), (22) are infinite. However, because we solve the coupled field equations numerically, we must truncate the sums at some $k = k_{\text{max}}$. We numerically determine this k_{max} for each of the sums at every (ℓ, m) such that the next term in the summation has absolute magnitude less than 10^{-14} . We also numerically check that each sum converges.

The coefficients a_k^i and b_k^i are unknown and must be determined by substituting our ansatz into the field equations then constructing recursion relations for the k^{th} coefficients a_k^i and b_k^i out of $a_{k' < k}^i$ and $b_{k' < k}^i$. The recursion relations for the outer BC for R_9^+ and R_{10}^+ are as follows:

$$2i\omega_k a_k^9 = C_{k-1} a_{k-1}^9 + D_{k-2} a_{k-2}^9 + E_{k-3} a_{k-3}^9 + 2a_{k-1}^{10} - 10M a_{k-2}^{10} + 12M^2 a_{k-3}^{10}, \quad (23)$$

$$2i\omega_k a_k^{10} = I_{k-1} a_{k-1}^{10} + J_{k-2} a_{k-2}^{10} + K_{k-3} a_{k-3}^{10} + 2\lambda a_{k-1}^9 - 4M\lambda a_{k-2}^9, \quad (24)$$

where

$$\begin{aligned} C_k &= 4Mi\omega k + k(k+1) - L - 4, & I_k &= 4Mi\omega k + k(k+1) - L + 2, \\ D_k &= -6Mk - 4Mk^2 + 24M + 2ML, & J_k &= -6Mk - 4Mk^2 - 6M + 2ML, \\ E_k &= 4M^2(k^2 + 2k - 8), & K_k &= 4M^2(k^2 + 2k + 1). \end{aligned}$$

Here and in all other recursion relations that we present, ω denotes $\omega_m = m\Omega_\phi$ and $L \equiv \ell(\ell + 1)$. The recursion relations are rather cumbersome, which is why we will refrain from presenting the rest of them in the main body of the paper unless we refer to them directly (as done in section III B 4). All the recursion relations are listed in appendix A.

The recursion relations must be started off by specifying the values for the leading terms. In the case of odd parity equations, these first terms are $a_0^{9,10}$ and $b_0^{9,10}$ with $a_{k<0}^{9,10} = 0$ and $b_{k<0}^{9,10} = 0$. This gives us 4 free parameters to specify every time we wish to solve the system of coupled ODEs. Since we have one gauge equation and three field equations for both inner and outer homogeneous solutions, we end up with $2 \times (3 - 1) = 4$ degrees of freedom. These d.o.f. are manifest in our freedom for choosing the values for $a_0^{9,10}$ and $b_0^{9,10}$. In the next subsection, we show how to pick suitable values for these coefficients and construct the inhomogeneous solutions.

The final remark concerns the nature of the BC specified above. As can be clearly seen, the ingoing/outgoing wave conditions for the BC yield complex numbers. Therefore, we must construct complex solutions for the homogeneous fields R_i^\pm . A quick inspection reveals that the real and imaginary part of the complex fields $R^{(i)}$ completely decouple in the field equations (19) and (20). As a result, we simply solve each given ODE twice: once with the real part of the BC and a 2nd time using the imaginary part of the BC. We then combine the two numerical homogeneous solutions under one complex solution that we also call R_i^\pm . Recall that we already have to solve the homogeneous ODEs twice to get the inner (-) and outer (+) solutions and now twice more for the real and imaginary parts. In total, at each generic odd mode, we must numerically solve the system of coupled ODEs $2 \times 4 = 8$ times.

1. Obtaining The Inhomogeneous Solutions

To obtain the true, inhomogeneous solutions — which are sourced by δ -functions — we must impose junction conditions on the coupled homogeneous solutions. Recalling that the inhomogeneous solutions $R^{(i)}$ must be C^0 fields, the two conditions are continuity at r_0 and the correct jump of $dR^{(i)}/dr$ across r_0 . Because we have coupled fields, we must construct the inhomogeneous solutions from linear combinations of homogeneous solutions. We use standard methods of constructing a linearly independent basis of homogeneous solutions and imposing the correct junction conditions to assemble the inhomogeneous fields. Below, we briefly outline this procedure.

As mentioned before, in the odd sector we have a total of 4 d.o.f. so we construct a 4-dimensional basis from the homogeneous solutions R_9^\pm and R_{10}^\pm . We do this by exploiting the freedom we have in choosing the initial values for the coefficients $a_{k=0}^{9,10}, b_{k=0}^{9,10}$ that start the recursion relations (23) - (24). A linearly independent 4-dimensional basis can be constructed for the homogeneous solutions $R_{9,10}$ by setting $(a_0^9, a_0^{10}) = (1, 0)$ then $(0, 1)$ and the same for (b_0^9, b_0^{10}) . These determine our basis vectors at the point of interest, namely $r = r_0$. We label these solutions by $R_9^{[1]\pm}, R_{10}^{[1]\pm}$ and $R_9^{[2]\pm}, R_{10}^{[2]\pm}$. For example, $R_9^{[1] +}, R_{10}^{[1] +}$ are obtained by setting $a_0^9 = 1$ and $a_0^{10} = 0$ then solving the coupled ODEs (19) and (20) for $R_9^+(r_0)$ and $R_{10}^+(r_0)$. Recall that since the boundary conditions are complex, the basis vectors are complex as well. Finally, we follow the same procedure for the r -derivatives. We label the inner and outer basis elements for the r -derivatives $\partial_r R_9^{[1]\pm}, \partial_r R_{10}^{[1]\pm}$ and $\partial_r R_9^{[2]\pm}, \partial_r R_{10}^{[2]\pm}$. So in this notation, $\partial_r R_{10}^{[2]-}$ stands for $dR_{10}^-/dr|_{r_0}$ obtained by setting $b_0^9 = 0$ and $b_0^{10} = 1$.

We label the inhomogeneous solutions by $R_{\text{in}}^{(i)}, R_{\text{out}}^{(i)}$. These are constructed from $R_{9,10}^{[j]+}, R_{9,10}^{[j]-}$ respectively. The inhomogeneous solutions are obtained by imposing the standard junction conditions: (1) Continuity at r_0 : $R_{\text{in}}^{(i)}(r_0) = R_{\text{out}}^{(i)}(r_0)$, (2) The following jump for the r -derivatives at r_0 :

$$\left. \frac{dR_{\text{out}}^{(i)}}{dr} \right|_{r_0} - \left. \frac{dR_{\text{in}}^{(i)}}{dr} \right|_{r_0} = -\frac{16\pi\mu\tilde{E}_0\alpha^{(i)}}{f_0^2} \times \mathcal{J}^{\text{odd}} \equiv J^{(i)}, \quad (i) = 9, 10, \quad (25)$$

where \mathcal{J}^{odd} is given by Eq. (11). To impose these conditions for our basis of homogeneous solutions, we form a 4×4 complex matrix containing the fields $R_i^{[j]\pm}, \partial_r R_i^{[j]\pm}$ listed above. The inhomogeneous solutions $R_{\text{in,out}}^{(9),(10)}$ are constructed from linear combinations of the homogenous solutions multiplied by unknown complex coefficients x_j . To

determine these coefficients, we must solve the following matrix equation:

$$\begin{pmatrix} -R_9^{[1]-} & -R_9^{[2]-} & R_9^{[1]+} & R_9^{[2]+} \\ -R_{10}^{[1]-} & -R_{10}^{[2]-} & R_{10}^{[1]+} & R_{10}^{[2]+} \\ -\partial_r R_9^{[1]-} & -\partial_r R_9^{[2]-} & \partial_r R_9^{[1]+} & \partial_r R_9^{[2]+} \\ -\partial_r R_{10}^{[1]-} & -\partial_r R_{10}^{[2]-} & \partial_r R_{10}^{[1]+} & \partial_r R_{10}^{[2]+} \end{pmatrix} \begin{pmatrix} x_1 \\ x_2 \\ x_3 \\ x_4 \end{pmatrix} = \begin{pmatrix} 0 \\ 0 \\ 0 \\ J^{(10)} \end{pmatrix} \quad (26)$$

The right hand side (RHS) of Eq.(26) ensures the continuity of the inhomogeneous solutions and imposes the correct jump value $J^{(i)}$ on the first derivatives. Recall that because $\alpha^{(9)} = 0$ (see Eq.(9)), we have $J^{(9)} = 0$. We solve for the complex x_1, \dots, x_4 by using standard numerical matrix inversion algorithms. Once we know the x_1, \dots, x_4 , we construct the inhomogeneous solutions at the location of the particle. These are given by

$$\begin{aligned} R_{\text{in}}^{(i)}(r_0) &= x_1 R_i^{[1]-} + x_2 R_i^{[2]-} + x_3 R_i^{[1]+} + x_4 R_i^{[2]+} = R_{\text{out}}^{(i)}(r_0), \\ \left. \frac{dR_{\text{in}}^{(i)}}{dr} \right|_{r_0} &= x_1 \partial_r R_i^{[1]-} + x_2 \partial_r R_i^{[2]-}, \quad \left. \frac{dR_{\text{out}}^{(i)}}{dr} \right|_{r_0} = x_3 \partial_r R_i^{[1]+} + x_4 \partial_r R_i^{[2]+}, \end{aligned} \quad (27)$$

where $i = 9, 10$. Although the continuity of $R^{(9)}, R^{(10)}$ and $dR^{(9)}/dr$ (because $J^{(9)} = 0$) is analytically exact, because the coupled ODEs are solved numerically, we will inevitably have a small violation of continuity at $r = r_0$. This is caused by the numerical matrix inversion. Usually, the numerical inversion algorithms are very robust and the discontinuity in the fields is $\sim 10^{-13} - 10^{-14}$ for most modes. However, for a few special modes, this error becomes much more significant. We will comment more on this issue later in section IV B.

We take the solutions (27) and substitute them into the odd gauge equation (18) to solve for $R^{(8)}(r_0)$. After this step, we obtain $dR^{(8)}/dr$ at $r = r_0$ by differentiating the gauge equation (18) with respect to r and using the field equation (19) to substitute for $\partial_r^2 R^{(9)}$ term in $dR^{(8)}/dr$. Recall that $R^{(8)}$ has a non-zero δ -function source thus it exhibits the standard jump discontinuity at r_0 given by Eq.(25). Therefore, we must compute $dR^{(8)}/dr|_{r_0}$ twice: once as $r \rightarrow r_0^+$ then again for $r \rightarrow r_0^-$. Since $R^{(8)}(r_0)$ and its \pm r -derivatives are obtained algebraically from Eq.(18) — by inserting the numerical solutions $R^{(9),(10)}(r_0)$, $dR^{(9),(10)}/dr|_{r_0}$ — we expect the error in the continuity of $R^{(8)}(r_0)$ to be comparable to errors found for $R^{(9),(10)}(r_0)$. Indeed, we find that the offset in the continuity of $R^{(8)}(r_0)$ is $\sim 10^{-13}$. Similarly, the relative error between $J^{(8)}$ and the jump of $dR^{(8)}/dr|_{r_0}$ is $\sim 10^{-14}$.

As mentioned above, we have to solve the set of coupled ODEs 8 times for each odd parity mode: twice owing to the fact the BC are complex, and 4 times because we construct the inhomogeneous solutions from a 4-dimensional basis of homogeneous solutions. Doing a run up to e.g. $\ell_{\text{max}} = 18$, we end up with 81 generic odd modes, which yield a total of $81 \times 8 = 648$ times that the coupled set of odd ODEs must be solved numerically.

2. The Static ($m = 0$) Odd Modes

As shown in BL, the $m = 0$ odd modes have analytic solutions. Since $J^{(10)} \propto m = 0$ and $J^{(9)} = 0$, we trivially have that $R^{(9)} = R^{(10)} = 0$ for these modes. Therefore, we solve a single ODE for $R^{(8)}$. For the case of $\ell = 1$, the ODE simplifies to a well known form, which has the following analytic solution:

$$R_{\ell=1}^{(8)}(r) = -\frac{1}{3} r_0 \beta_{\ell=1} \times \begin{cases} (r/r_0)^2, & r \leq r_0 \\ (r_0/r), & r \geq r_0, \end{cases} \quad (29)$$

where $\beta_{\ell=1} = 16\sqrt{3\pi} f_0^{-1} \tilde{E}_0 \Omega_0$. For $\ell > 1$, the inner ($r < r_0$) homogeneous solutions exhibit the standard power law behavior: $\sim r^{\ell+1}$. As for the outer solutions ($r > r_0$), we have something that is of the form $r^{-\ell}(1 + \ln f)$. These scale as $r^{-\ell}$ as $r \rightarrow \infty$, which is regular. The details of how these analytic solutions are constructed are given in section IIIC of BL, which is why we refrain from elaborating more here. We also omit the explicit expressions for these static, $\ell > 1$ solutions in this article. The interested reader should peruse BL ([20]). In summary, the overall static, odd solutions are given by — restoring the modal indices — $\bar{h}^{(9)\ell 0} = \bar{h}^{(10)\ell 0} = 0$ and the non-zero fields $\bar{h}^{(8)\ell 0}$, which are constructed analytically.

B. Even Sector

For the generic, non-static case of even modes, we have 7 field and 3 gauge equations thus a total of $2 \times (7 - 3) = 8$ d.o.f. However, an inspection of the even parity field equations as they are written in Lorenz gauge ([1], [20], [32])

reveals that we must simultaneously solve 5, not 4, coupled ODEs. As before, we numerically solve the homogeneous ODEs then obtain the inhomogeneous solutions by employing the standard techniques for coupled fields, which we illustrated in section III A 1. The 5 homogeneous coupled ODEs in the even sector are the $(i) = 1, 3, 5, 6, 7$ equations written in the following form:

$$\partial_{r_*}^2 R^{(1)} = 4V_{\ell m} R^{(1)} + \frac{4M}{r^2} f R_{,r_*}^{(3)} + \frac{2f}{r^2} \left(1 - \frac{4M}{r}\right) (R^{(1)} - R^{(5)} - f R^{(3)}) - \frac{2f^2}{r^2} \left(1 - \frac{6M}{r}\right) R^{(6)}, \quad (30)$$

$$\partial_{r_*}^2 R^{(3)} = 4V_{\ell m} R^{(3)} - \frac{2f}{r^2} \left[R^{(1)} - R^{(5)} - \left(1 - \frac{4M}{r}\right) (R^{(3)} + R^{(6)}) \right], \quad (31)$$

$$\partial_{r_*}^2 R^{(5)} = 4V_{\ell m} R^{(5)} + \frac{4f}{r^2} \left[\left(1 - \frac{4.5M}{r}\right) R^{(5)} - \frac{L}{2} (R^{(1)} - f R^{(3)}) + \frac{1}{2} \left(1 - \frac{3M}{r}\right) (L R^{(6)} - R^{(7)}) \right], \quad (32)$$

$$\partial_{r_*}^2 R^{(6)} = 4V_{\ell m} R^{(6)} - \frac{2f}{r^2} \left[R^{(1)} - R^{(5)} - \left(1 - \frac{4M}{r}\right) (R^{(3)} + R^{(6)}) \right], \quad (33)$$

$$\partial_{r_*}^2 R^{(7)} = 4V_{\ell m} R^{(7)} - \frac{2f}{r^2} (R^{(7)} + \lambda R^{(5)}). \quad (34)$$

In this article, we follow the convention of BS [32] for the field $\bar{h}^{(3)}$, which is different from that of BL [20]: $\bar{h}_{here}^{(3)} = \bar{h}_{BL}^{(3)}/f$. Recall that $f = 1 - 2M/r$, $L \equiv \ell(\ell + 1)$, $\lambda = (\ell + 2)(\ell - 1)$ and $V_{\ell m}$ is given by Eq. (14). Next, we must specify the boundary conditions. As was the case with the odd sector fields, we impose the same ingoing/outgoing wave conditions on the event horizon and at radial infinity, respectively. We once again use R_i^-, R_i^+ to denote the ingoing, outgoing homogeneous solutions, respectively. For the inner/outer BC, we use the same ansatz as before

$$R_i^- = e^{-i\omega_m r_*} \sum_{k=0}^{\infty} b_k^i (r - 2M)^k, \quad (35)$$

$$R_i^+ = e^{i\omega_m r_*} \sum_{k=0}^{\infty} \frac{a_k^i}{r^k} \quad (36)$$

for $i = 1, 3, 5, 6, 7$. Once again, we substitute these ansatz into the field equations (30) - (34) to derive new recursion relations for the coefficients a_k^i, b_k^i in Eqs. (35), (36). The sums are of course infinite but we truncate them at some $k = k_{\max}$ as we did before. The recursion relations for the outer coefficients a_k^i and inner coefficients b_k^i are given in appendix A.

With the coefficients a_k^i, b_k^i determined, there still remains one critical issue that pertains to the total number of degrees of freedom to use: in the even sector, we have 5 ODEs that can not be decoupled from each other, so we must solve all five simultaneously, but we have 8 d.o.f in the even sector, not $2 \times 5 = 10$. So, there must be an extra condition on each set of 5 BC for inner and outer homogeneous solutions. For the outer solutions, this extra condition is a constraint on the coefficients a_k^3 , which is given by the even gauge equations:

$$a_0^3 = 0. \quad (37)$$

We repeat this procedure of eliminating the 5th degree of freedom from the inner homogeneous solutions by making use of the gauge equations. After some manipulation, we reach the following condition on the coefficients b_k^3 :

$$b_0^3 = - \frac{[(i\ell(\ell + 1) + 4M\omega(1 - 4M i\omega + \ell(\ell + 1)))] b_0^1 + i(1 + 16M^2\omega^2) b_0^5}{2M\omega(1 + 16M^2\omega^2)}. \quad (38)$$

So all of the coefficients b_k^3 are entirely determined from b_0^1, b_0^5 and the recursion relation (A22). With the conditions (37) and (38) imposed, we are left with the expected 8 d.o.f.

Eqs.(37) and (38) tell us that our 8-dimensional basis of inner and outer homogeneous solutions is constructed by using the recursion relations (A6) - (A29) for the BC with $\{b_0^1, b_0^5, b_0^6, b_0^7\}$ and $\{a_0^1, a_0^5, a_0^6, a_0^7\}$ as the sets containing the 8 free parameters for the inner and outer homogeneous solutions. We construct our basis of linearly independent homogeneous solutions by numerically determining the basis vectors that span the solution space. Each basis vector of the outer homogeneous solution space is obtained by setting one of the coefficients $\{a_0^1, a_0^5, a_0^6, a_0^7\}$ equal to 1 while the other 3 equal 0. We do this a total of 4 times, e.g. $\{a_0^1, a_0^5, a_0^6, a_0^7\} = \{1, 0, 0, 0\}, \{0, 1, 0, 0\}, \{0, 0, 1, 0\}$ and $\{0, 0, 0, 1\}$. This procedure is repeated with $\{b_0^1, b_0^5, b_0^6, b_0^7\}$ for the inner solutions. This yields 8 basis vectors for constructing the 8-dimensional linearly independent homogeneous solution space. Given that the system of ODEs must be solved

twice because the BC are complex, we reach a total of $8 \times 2 = 16$ for the number of times we must numerically solve the field equations at each *even* mode. For example, for ℓ running up to 18, we have a total of 89 generic even modes, which means that the coupled ODEs are numerically integrated a total of $89 \times 16 = 1424$ times. This is what takes up the main bulk of our numerical computation time. We will say more about this later. Next, we construct the inhomogeneous solutions.

1. Inhomogeneous Solutions

In subsection III A 1, we showed in detail how to construct the inhomogeneous solutions from the inner and outer homogeneous solutions. Here we do the same with the even parity solutions. Our basis of homogeneous solutions is now 8-dimensional and is spanned by $R_i^\pm, \partial_r R_i^\pm$ with $i = 1, 5, 6, 7$. In accordance with the notation of subsection III A 1, we label the basis vectors (the homogeneous fields $R_{1,5,6,7}^\pm$) by $R_i^{[j]\pm}$. Similarly, for the derivatives, we use $\partial_r R_i^{[j]\pm}$. For example, $R_1^{[1]+}$ stands for R_1^+ obtained by setting $a_0^1 = 1$ and $a_0^5 = a_0^6 = a_0^7 = 0$ and $\partial_r R_6^{[3]-}$ is dR_6^-/dr with $b_0^6 = 1$ and $b_0^1 = b_0^5 = b_0^7 = 0$.

To construct the inhomogeneous solutions, we impose the junction conditions on the homogeneous fields and their r -derivatives in the form of an 8-dimensional complex matrix equation:

$$\left(\begin{array}{c|c} -R_i^{[j]-} & R_i^{[j]+} \\ \hline -\partial_r R_i^{[j]-} & \partial_r R_i^{[j]+} \end{array} \right) \begin{pmatrix} x_1 \\ \vdots \\ x_8 \end{pmatrix} = \begin{pmatrix} 0_{4 \times 1} \\ J^{(i)} \end{pmatrix}. \quad (39)$$

$0_{4 \times 1}$ is a 4×1 array of zeros imposing the condition of continuity for the inhomogeneous fields $R^{(i)}$ and

$$J^{(i)} \equiv -\frac{16\pi\mu\tilde{E}_0\alpha^{(i)}}{f_0^2} \hat{c}_{\ell m} P^{\ell m}(\theta = \pi/2). \quad (40)$$

The complex, inhomogeneous fields $R^{(i)}$ at $r = r_0$ are given by

$$R_{\text{in}}^{(i)}(r_0) = \sum_{j=1}^4 x_j R_i^{[j]-} = \sum_{j=1}^4 x_{j+4} R_i^{[j]+} = R_{\text{out}}^{(i)}(r_0). \quad (41)$$

Similarly, for the r -derivatives of these fields at $r = r_0$, we have

$$\left. \frac{dR_{\text{in}}^{(i)}}{dr} \right|_{r_0} = \sum_{j=1}^4 x_j \partial_r R_i^{[j]-} \quad (42)$$

$$\left. \frac{dR_{\text{out}}^{(i)}}{dr} \right|_{r_0} = \sum_{j=1}^4 x_{j+4} \partial_r R_i^{[j]+}. \quad (43)$$

We still need to determine the inhomogeneous field $R^{(3)}$ and its r -derivative at r_0 . Recall that in order to form the linearly independent basis of homogeneous solutions we had to solve a system of 5 (not 4) coupled ODEs together. However, the homogeneous solutions R_3^\pm and their first derivatives $R_3^{\prime\pm}$ are not part of our basis because they are constructed from linear combinations of the other basis elements as shown in Eqs. (37) & (38). With the basis of homogenous solutions at hand, $R^{(3)}(r_0), dR^{(3)}/dr|_{r_0}$ are simply given by

$$R_{\text{out}}^{(3)}(r_0) = \sum_{j=1}^4 x_j R_3^{[j]-} = \sum_{j=1}^4 x_{j+4} R_3^{[j]+} = R_{\text{out}}^{(3)}(r_0), \quad (44)$$

$$\left. \frac{dR_{\text{in}}^{(3)}}{dr} \right|_{r_0} = \sum_{j=1}^4 x_j \partial_r R_3^{[j]-}, \quad (45)$$

$$\left. \frac{dR_{\text{out}}^{(3)}}{dr} \right|_{r_0} = \sum_{j=1}^4 x_{j+4} \partial_r R_3^{[j]+}. \quad (46)$$

The remaining two fields $R^{(2)}$ and $R^{(4)}$ are extracted from the even parity gauge equations (16), (17). Their r -derivatives are obtained by differentiating these gauge equations with respect to r and substituting the relevant parts of the fields equations ($i = 1, 3, 5$ for the $\partial_r^2 R^{(1)}, \partial_r^2 R^{(3)}, \partial_r^2 R^{(5)}$ terms that arise from r -derivatives of Eqs. (16), (17).

Although $R_{\text{in}}^{(i)}(r_0) = R_{\text{out}}^{(i)}(r_0)$ analytically, because we invert the complex matrix numerically, we are bound to have small discontinuities at r_0 as we did with the odd parity fields. We checked the relative error in the continuity of the fields $R^{(1)}, \dots, R^{(7)}$ at $r = r_0$ and found that it is at most $\mathcal{O}(10^{-12})$ for $r_0 \lesssim 100M$ and $\ell - m = \text{small}$. However, we find that for $r_0 > 100M$, as $\ell - m \rightarrow 15$, the violation of the continuity of the field $R^{(5)}$ grows up to $\mathcal{O}(10^{-7})$ in relative size. For $\ell - m \gtrsim 30$, this violation climbs up to $\mathcal{O}(10^{-5})$. Clearly, for large orbital radii and large $\ell - m$, the numerical matrix inversion becomes less accurate. A quick check of condition numbers c for the matrices in Eq. (39) shows that $c \gtrsim 10^{12}$ for the problematic cases mentioned here. We explain the cause of this in section IV B. However, it is only the field $R^{(5)}$ that exhibits the bad discontinuities; the fields $R^{(1),(6),(7)}$, which also come directly out of the matrix inversion, have continuity violations that are consistently at least three or more orders of magnitude smaller. As expected, larger inversion errors persist in the fields $R^{(2)}, R^{(4)}$ (and their r -derivatives) because these are constructed from gauge equations containing $R^{(5)}$ and its first and second r -derivatives. As far as we can tell this matrix inversion error, which we quantify by the numerical discontinuity of the fields $R^{(2),(4),(5)}$ at $r = r_0$ is our largest source of error. We will say more on this inversion error in section IV B.

2. The Even Dipole ($\ell = 1, m = 1$) Mode

The even parity dipole mode is non-radiative ($\ell < 2$) thus represents a shift in the orbital angular momentum, which can be interpreted as a rotation of spacetime around its center of mass. For $\ell = 1, m = 1, \lambda = 0$ as well as $\alpha^{(7)} = J^{(7)} = 0$. This gives $\bar{h}^{(7)11}(t, r) = 0$, which results in 4 coupled ODEs. The ($i = 1, 3, 6$) equations (30), (31), (33) do not contain any $R^{(7)}$ terms as such they remain unchanged, as do the recursion relations for $a_k^{1,3,6}, b_k^{1,3,6}$ displayed in appendix A 1. However the ($i = 5$) equation (32) does contain a $\lambda R^{(7)}$ term, which is now zero so we end up with new recursion relations for the inner and outer boundary conditions for R_5^\pm . These are given by Eqs. (A31), (A32) in appendix A 2.

With $R_7^\pm = 0$, we have $2 \times (6 - 3) = 6$ degrees of freedom for our basis of homogeneous solutions. The basis vectors are constructed from the homogeneous solutions obtained by using the BC generated from the sets $\{b_0^1, b_0^5, b_0^6\}$ and $\{a_0^1, a_0^5, a_0^6\}$, respectively. The ODE integrator solves the coupled system a total of $2 \times 6 = 12$ times. To obtain the inhomogeneous solutions, we construct a 6×6 complex matrix very similar to the one in Eq.(39), but without the homogeneous fields $R_7^{[j]\pm}, \partial_r R_7^{[j]\pm}$. We solve the resulting matrix equation to obtain the values for the complex amplitudes x_1, \dots, x_6 , which in turn, give us the values of the inhomogeneous solutions and their first r -derivatives at r_0 . The equations for the inhomogeneous fields $R^{(1),(3),(5),(6)}(r_0)$ are identical to Eq. (41), (44) with $x_7 = x_8 = 0$. The fields $R^{(2),(4)}(r_0)$ are once again obtained from the gauge equations (16) and (17) with $R^{(7)} = 0$.

3. The Monopole $\ell = 0$ Mode

This conservative, non-radiative $\ell = 0$ contribution to the metric perturbations represents a shift in the mass of the small particle across $r = r_0$. For this mode, the field equations simplify enough that analytic solutions have been found by Detweiler & Poisson [33]. The only non-zero fields are $\bar{h}^{(1)} = R^{(1)}, \bar{h}^{(3)} = R^{(3)}, \bar{h}^{(6)} = R^{(6)}$, which contribute only to the diagonal (scalar) components of $h_{\mu\nu}$. In section III.D of BL, the solutions are displayed explicitly in terms of the components of $h_{\mu\nu}$. As with the other modes, these are C^0 with the usual jump in the r -derivative across r_0 . We omit writing the explicit solutions here and refer the interested reader to [20], section III.D for the details. The extra important step we mention here is the rewriting of these analytic solutions — written as components of $h_{\mu\nu}$ in BL — in terms of $\bar{h}^{(i)}$. Although this seems like a backward step, it is necessary in order to properly follow the algorithm for computing the GSF. We will elaborate more on this procedure later in section IV.

The formulae needed to transform $h_{tt}, h_{rr}, h_{\theta\theta}, h_{\phi\phi}$ to $\bar{h}^{(1)}, \bar{h}^{(3)}, \bar{h}^{(6)}$ are as follows ([20]):

$$\bar{h}_{\ell=0}^{(1)}(r) = 2\sqrt{\pi}\mu^{-1}r(h_{tt} + f^2 h_{rr}), \quad (47)$$

$$\bar{h}_{\ell=0}^{(6)}(r) = 2\sqrt{\pi}\mu^{-1}\frac{r}{f}(h_{tt} - f^2 h_{rr}), \quad (48)$$

$$\bar{h}_{\ell=0}^{(3)}(r) = 4\sqrt{\pi}\mu^{-1}r^{-1}h_{\theta\theta} = 4\sqrt{\pi}\mu^{-1}r^{-1}(\sin\theta)^{-2}h_{\phi\phi}. \quad (49)$$

Note that the expression for $\bar{h}^{(3)}$ here looks different from the one given by BL in [20]. The reader may recall that this is because we use the $\bar{h}^{(3)}$ as defined by BS in [32] as opposed to BL as was mentioned earlier. From these relations

and the explicit expressions provided for $\bar{h}^{(1),(3),(6)}$ in [20], it is straightforward to evaluate the fields $\bar{h}^{(i)}$ and their inner and outer r -derivatives at $r = r_0$, which then give us the total contribution of the monopole ($\ell = 0$) to the GSF.

4. The Even Static Modes ($\ell \geq 2(\text{even}), m = 0$)

These modes require a special discussion not only because the dimension of the homogeneous solutions space is smaller but also because the BC require extra care. With $m = 0$, we have that $\alpha^{(2)} = 0$ and $\alpha^{(4)} = 0$. Furthermore, an inspection of $tr, t\theta, t\phi$ components of $h_{\mu\nu}$ (cf. Eq.(20) of [20]) reveals that these depend only on $\bar{h}^{(2)}$ and $\bar{h}^{(4)}$. Since static modes must be symmetric under time reversal, we have that $h_{ti} = 0$ for $i = r, \theta, \phi$ thus we must have $\bar{h}^{(2)} = 0$ and $\bar{h}^{(4)} = 0$ for the static, even modes. This reduces the total number of fields in the even sector to 5 and eliminates the gauge equation (15) (it gives the trivial $0 = 0$). Using the remaining two gauge equations (16), (17), we can obtain expressions for $R^{(6),(7)}$ in terms of $R^{(1),(3),(5)}$. We then substitute these into the field equations (30) - (32). This yields modified field equations for $(i) = 1, 3, 5$:

$$\begin{aligned} \partial_{r_*}^2 R^{(1)} &= 4V_{\ell m} R^{(1)} + \frac{4M}{r^2} f \partial_{r_*} R^{(3)} + \frac{2f}{r^2} \left(1 - \frac{4M}{r}\right) \left(R^{(1)} - R^{(5)} - fR^{(3)}\right) \\ &\quad - \frac{f}{r^2} \left(1 - \frac{6M}{r}\right) \left[R^{(1)} + \frac{r}{f} \partial_{r_*} R^{(1)} - fR^{(3)} - r \partial_{r_*} R^{(3)} - R^{(5)}\right], \end{aligned} \quad (50)$$

$$\begin{aligned} \partial_{r_*}^2 R^{(3)} &= 4V_{\ell m} R^{(3)} \\ &\quad - \frac{2f}{r^2} \left\{ R^{(1)} - R^{(5)} - \left(1 - \frac{4M}{r}\right) \left[R^{(3)} + \frac{1}{2f} \left(R^{(1)} + \frac{r}{f} \partial_{r_*} R^{(1)} - fR^{(3)} - r \partial_{r_*} R^{(3)} - R^{(5)} \right) \right] \right\}, \end{aligned} \quad (51)$$

$$\begin{aligned} \partial_{r_*}^2 R^{(5)} &= 4V_{\ell m} R^{(5)} \\ &\quad + \frac{4f}{r^2} \left[\left(1 - \frac{4.5M}{r}\right) R^{(5)} - \frac{\ell(\ell+1)}{2} \left(R^{(1)} - fR^{(3)}\right) - \frac{1}{2} \left(1 - \frac{3M}{r}\right) \left(2R^{(5)} + \frac{r}{f} \partial_{r_*} R^{(5)}\right) \right]. \end{aligned} \quad (52)$$

Next, we calculate the boundary conditions for the static homogeneous solutions $R_{1,3,5}^\pm$. Because we are looking at static modes, the ingoing/outgoing wave conditions are no longer appropriate for the BC. Our determining criterion is now regularity, so for the inner homogeneous solutions R_i^- , we select the following ansatz:

$$R_i^- = \sum_{k=k_{\text{start}}}^{\infty} b_k^i (r - 2M)^k. \quad (53)$$

Substituting the ansatz (53) into the field equations for $(i) = 1, 3, 5$ gives us new recursion relations for the BC, which we display explicitly below as we will be making remarks about them here. We also list them in appendix A 3.

$$\begin{aligned} 8M^3 k(k-2)b_k^1 &= \bar{F}_{k-1}^1 b_{k-1}^1 + \bar{G}_{k-2}^1 b_{k-2}^1 + \bar{G}_{k-2}^3 b_{k-2}^3 - 2M b_{k-2}^5 \\ &\quad + \bar{E}_{k-3}^3 b_{k-3}^1 + \bar{E}_{k-3}^1 b_{k-3}^3 - b_{k-3}^5, \end{aligned} \quad (54)$$

$$\begin{aligned} 4Mk(k-1)b_k^5 &= \bar{C}_{k-1}^5 b_{k-1}^5 - 4ML b_{k-1}^1 + \bar{D}_{k-2}^5 b_{k-2}^5 + 2L(b_{k-2}^3 - b_{k-2}^1), \\ \bar{C}_{k-1}^3 b_{k-1}^3 &= \bar{C}_{k-1}^1 b_{k-1}^1 - 8M^3 k b_k^1 + 4M^2 b_{k-1}^5 + \bar{D}_{k-2}^3 b_{k-2}^3 + \bar{D}_{k-2}^1 b_{k-2}^1 \\ &\quad + 4M b_{k-2}^5 + \bar{E}_{k-3}^3 b_{k-3}^3 + \bar{E}_{k-3}^1 b_{k-3}^1 + b_{k-3}^5, \end{aligned} \quad (55)$$

where

$$\bar{C}_k^1 = -4M^2(k+1), \quad \bar{C}_k^3 = 4M^2 k(k-1), \quad \bar{C}_k^5 = 2ML - 4M(1+k^2) \quad (56)$$

$$\bar{D}_k^1 = 2M(k-2), \quad \bar{D}_k^3 = 2M(L+k(1-2k)), \quad \bar{D}_k^5 = L - k(k+1), \quad (57)$$

$$\bar{E}_k^1 = L + 1 - k^2, \quad \bar{E}_k^3 = k - 1, \quad \bar{G}_k^3 = 2Mk, \quad (58)$$

$$\bar{F}_k^1 = 4M^2(L+1+4k-3k^2), \quad \bar{G}_k^1 = 2M(2L+2+2k-3k^2). \quad (59)$$

Little care is needed when evaluating the coefficients b_k^1, b_k^3 using the recursion relations (54) and (55). First, because the left-hand-side of Eq.(54) gives zero for $k = 0, 2$ we must start this recursion relation at $k = 3$ with $b_0^1 = b_1^1 = 0$. Similarly, the recursion relation for b_k^5 starts at $k = 2$ with $b_0^5 = 0$ and b_1^5 as the free parameter. Further inspection reveals that the remaining two free parameters are b_0^3, b_1^3 . This can be seen by realizing that $\bar{C}_k^3 = 0$ for $k = 1$ so we can not use the recursion relation (55) until $k = 2$ but we need b_0^3 and b_1^3 to determine $b_{k \geq 2}^1$ in Eq.(54) and $b_{k \geq 2}^5$ in Eq.(55). So our 3-dimensional basis of homogeneous solutions is generated from the set $\{b_0^3, b_1^3, b_1^5\}$. When we evaluate

these three recursion relations to obtain the higher-k coefficients, we first get b_k^1, b_k^5 then at the $(k+1)^{\text{th}}$ order we recover b_k^3 . For example, at $k=2$ we obtain b_2^1, b_2^5 then at $k=3$ we recover b_2^3 and also obtain b_3^1, b_3^5 . As usual, we truncate the infinite sum at some $k = k_{max}$ such that the contribution of $(k_{max}+1)^{\text{th}}$ term has absolute magnitude less than 10^{-14} .

Next, we turn to determining the outer boundary conditions. This particular case is more involved than all the other BC thus far mentioned. First of all, the naive ansatz of $R_i^+ = \sum_k a_k^i / r^k$ only provides two free parameters thus falls one short of the needed three d.o.f. for the outer solutions. Inspired by the analytic, outer homogeneous solutions for $\ell = \text{odd}, m = 0$ modes, which have $r^{-\ell}, r^{-\ell} \ln r$ large- r behavior, we make the following ansatz

$$R_i^+ = \sum_{k=k_{\text{start}}}^{\infty} \frac{a_k^i + \bar{a}_k^i \ln r}{r^k}. \quad (60)$$

When we substitute this ansatz into the ODEs (50), (51), (52), we find that $a_k^i = 0$ for all $k < \ell$. Two of the three free parameters are $a_{k=\ell}^3, a_{k=\ell}^5$ which combine to give

$$a_\ell^1 = a_\ell^3 + \frac{a_\ell^5}{\ell+1}. \quad (61)$$

The next order terms in the recursion relations are as follows

$$\begin{aligned} a_{\ell+1}^1 &= \frac{1}{4L} [2L(2+\ell)a_\ell^1 - 4La_\ell^3 + 2(2-\ell^2)a_\ell^5], \\ a_{\ell+1}^3 &= \frac{1}{4L} [2L(\ell-2)a_\ell^1 + 12La_\ell^3 + 2(\ell(\ell+2)-2)a_\ell^5], \\ a_{\ell+1}^5 &= \ell a_{\ell+1}^3 + (\ell+2)a_{\ell+1}^1 - 2(\ell^2 - \ell - 2)a_\ell^3 - 4a_\ell^1. \end{aligned}$$

Note that all of these still only depend on the 2 free parameters a_ℓ^3, a_ℓ^5 . It turns out the third free parameter is $a_{\ell+2}^5$. As for the \bar{a}_k^i , they are all given in terms of $\{a_\ell^3, a_\ell^5, a_{\ell+2}^5\}$ with the condition $\bar{a}_{k<\ell+2}^i = 0$. Unlike the previous cases, here we get two sets of recursion relations from each field equation, one for a_k^i and another for \bar{a}_k^i . These are:

$$\begin{aligned} \hat{C}_k^1 a_k^1 &= (k+1)a_k^3 + a_k^5 - 2k\bar{a}_k^1 - \bar{a}_k^3 \\ &\quad - 2M \left(\hat{D}_{k-1}^1 a_{k-1}^1 + \hat{D}_{k-1}^3 a_{k-1}^3 + a_{k-1}^5 + \hat{E}_{k-1}^1 \bar{a}_{k-1}^1 - 2\bar{a}_{k-1}^3 \right) \\ &\quad + 4M^2 \left(\hat{F}_{k-2}^3 a_{k-2}^3 - \bar{a}_{k-2}^3 \right), \end{aligned} \quad (62)$$

$$\begin{aligned} \hat{C}_k^1 \bar{a}_k^1 &= (k+1)\bar{a}_k^3 + \bar{a}_k^5 - 2M \left(\hat{D}_{k-1}^1 \bar{a}_{k-1}^1 + \hat{D}_{k-1}^3 \bar{a}_{k-1}^3 + \bar{a}_{k-1}^5 \right) \\ &\quad + 4M^2 \hat{F}_{k-2}^3 \bar{a}_{k-2}^3, \end{aligned} \quad (63)$$

where

$$\begin{aligned} \hat{C}_k^1 &= L+1-k^2, & \hat{D}_k^1 &= k(k-1), & \hat{D}_k^3 &= 2(k+1), \\ \hat{E}_k^1 &= 1-2k, & \hat{F}_k^3 &= k+1. \end{aligned}$$

$$\begin{aligned} \hat{C}_k^1 a_k^3 &= (k+1)a_k^1 - a_k^5 - \bar{a}_k^1 - 2k\bar{a}_k^3 \\ &\quad - 2M \left(\hat{G}_{k-1}^3 a_{k-1}^3 + \hat{G}_{k-1}^1 a_{k-1}^1 + \hat{H}_{k-1}^3 \bar{a}_{k-1}^3 - 2\bar{a}_{k-1}^1 \right) \\ &\quad + 4M^2 \left(\hat{I}_{k-2}^3 a_{k-2}^3 + \hat{J}_{k-2}^3 \bar{a}_{k-2}^3 \right), \end{aligned} \quad (64)$$

$$\begin{aligned} \hat{C}_k^1 \bar{a}_k^3 &= (k+1)\bar{a}_k^1 - \bar{a}_k^5 - 2M \left(\hat{G}_{k-1}^3 \bar{a}_{k-1}^3 + \hat{G}_{k-1}^1 \bar{a}_{k-1}^1 \right) \\ &\quad + 4M^2 \hat{I}_{k-2}^3 \bar{a}_{k-2}^3, \end{aligned} \quad (65)$$

where

$$\begin{aligned} \hat{G}_k^3 &= 2k^2 - 2 - L, & \hat{G}_k^1 &= 2k, & \hat{H}_k^3 &= -4k, \\ \hat{I}_k^3 &= k^2 - 1, & \hat{J}_k^3 &= -2k. \end{aligned}$$

$$\hat{C}_k^5 a_k^5 = 2L(a_k^1 - a_k^3) - \hat{D}_k^5 \bar{a}_k^5 + 2M \left(\hat{E}_{k-1}^5 a_{k-1}^5 + 2L a_{k-1}^3 + \hat{D}_{k-1}^5 \bar{a}_{k-1}^5 \right), \quad (66)$$

$$\hat{C}_k^5 \bar{a}_k^5 = 2L(\bar{a}_k^1 - \bar{a}_k^3) + 2M \left(\hat{E}_{k-1}^5 \bar{a}_{k-1}^5 + 2L \bar{a}_{k-1}^3 \right), \quad (67)$$

where

$$\hat{C}_k^5 = L + k(1 - k), \quad \hat{D}_k^5 = 2k - 1, \quad \hat{E}_k^5 = k(1 - k) + 2.$$

The careful reader will note that the recursion relations appear coupled to each other in Eqs. (62) - (67). That is, unlike all other recursion relations, the right-hand-sides of Eqs. (62) - (67) contain k^{th} order terms. If we move all order k terms to the left-hand-sides of Eqs. (62) - (67), we find that the LHSs form a coupled system of 6 equations with 6 unknowns. These equations are ‘uncoupled’ by using standard linear algebra methods. This naturally leads to the RHSs transforming into rather cumbersome expressions so we omit displaying them here.

With the boundary conditions for the inner and outer homogeneous solutions computed, we numerically solve the coupled set of three ODEs as before. The vector space of linearly independent homogeneous solutions is now 6-dimensional and is constructed from inner, outer homogeneous solutions generated using BC obtained from the sets $\{b_0^3, b_1^3, b_1^5\}$ for the inner and $\{a_\ell^3, a_\ell^5, a_{\ell+2}^5\}$ for the outer solutions, respectively. So at each $(\ell \geq 2, m = 0)$ even mode, we numerically integrate the ODEs for a total of $2 \times 6 = 12$ times. To determine the inhomogeneous solutions $R^{(1),(3),(5)}(r_0)$ and their inner/outer r -derivatives, we construct a 6×6 complex matrix and invert it to solve for the complex amplitudes x_1, \dots, x_6 as before. We omit the details here as we have illustrated how to do this for both the generic odd and even modes in sections III A 1, III B 1 respectively. Once these fields are known, we can then use the gauge equations to construct $R^{(6)}(r_0)$ and $R^{(7)}(r_0)$ and their inner/outer r -derivatives at $r = r_0$.

IV. COMPUTING THE GRAVITATIONAL SELF-FORCE

With all the metric fields $\bar{h}^{(i)}$ and their t, r -derivatives computed, we now focus on the actual calculation of the gravitational self-force. We follow the prescription of [1] and [32].

Because we are modeling the small mass μ as a point particle, we are faced with the issue of the divergence of the GSF at the location of the particle. This requires a careful regularization of the GSF to remove the divergent, but non-physical, piece from it. We can write the regularized GSF as [17]

$$F^\alpha(x_0) = \lim_{x \rightarrow x_0} [F_{\text{full}}^\alpha(x) - F_{\text{dir}}^\alpha(x)], \quad (68)$$

where F_{full}^α is the ‘‘full’’ GSF constructed from the metric perturbation, and F_{dir}^α is the ‘‘direct’’ (divergent) piece of it. Physically speaking, F_{dir}^α can be thought of as representing the instantaneous part of the GSF that propagates along the past light-cone of the particle.

In the mode-sum scheme, F_{full}^α and F_{dir}^α are decomposed into multipole modes $F_{\text{full}}^{\alpha l}$ and $F_{\text{dir}}^{\alpha l}$. Thanks to this multipole expansion, the individual l -modes of the divergent piece $F_{\text{dir}}^{\alpha l}$ all have finite values at the $x^\mu \rightarrow x_0^\mu$ limit. l here represents the scalar spherical harmonic modes and it should not be confused with the tensorial modal index ℓ of the previous sections.

Individual l -modes of F_{full}^α are obtained from the fields $\bar{h}^{(i)\ell m}$ and their derivatives as given by Eq.(72) below. Then the GSF at the location of the particle (x_0) is given by

$$F^\alpha(x_0) = \sum_{l=0}^{\infty} ([F_{\text{full}}^{\alpha l}(x_0)]_{\pm} - A_{\pm}^{\alpha} L_{1/2} - B^{\alpha}) \equiv \sum_{l=0}^{\infty} [F_{\text{reg}}^{\alpha l}(x_0)]_{\pm}, \quad (69)$$

where $L_{1/2} \equiv l + 1/2$. The \pm correspond to taking the r -derivative at the $r \rightarrow r_0^{\pm}$ limit. A_{\pm}^{α} and B^{α} are regularization parameters. They are derived from the local structure of $F_{\text{dir}}^{\alpha l}$ near $x_0^{\mu \pm}$. $\mp A_{\pm}^{\alpha} L_{1/2} + B^{\alpha}$ represents the asymptotic form of $F_{\text{dir}}^{\alpha l}$ for large l . For circular orbits in Schwarzschild spacetime, $A_{\pm}^{\alpha} = B^{\alpha} = 0$ for $\alpha = t, \theta, \phi$. The non-zero r -components are given by [17]

$$A_{\pm}^r = \mp \frac{\mu^2}{r_0^2} \left(1 - \frac{3M}{r_0} \right)^{1/2}, \quad (70)$$

$$B^r = \frac{\mu^2 r_0 \tilde{E}_0^2}{\pi (\tilde{L}_0^2 + r_0^2)^{3/2}} \left[\hat{E}(w) - 2\hat{K}(w) \right], \quad (71)$$

where $\tilde{L}_0 = (Mr_0)^{1/2}/(1-3M/r_0)^{1/2}$ is the orbital angular momentum, $\hat{K}(w) \equiv \int_0^{\pi/2} (1-w \sin^2 x)^{-1/2} dx$ and $\hat{E}(w) \equiv \int_0^{\pi/2} (1-w \sin^2 x)^{1/2} dx$ are the complete elliptic integrals of first and second kind, respectively and $w \equiv (r_0/M - 2)^{-1}$. The regularized GSF can be computed by using either one of the \pm values: the quantity $F_{\text{full}}^{\alpha l \pm} - L_{1/2} A_{\pm}^{\alpha}$ is direction independent. This \pm equality provides us with a way to check our GSF results. Since the t -component needs no regularization, we can write $F_{\text{reg}}^{t l \pm} = F_{\text{full}+}^{t l} = F_{\text{full}-}^{t l}$.

The l modes of the full force are given by [32]

$$[F_{\text{full}}^{\alpha l}(x_0)]_{\pm} = \frac{\mu^2}{r_0^2} \sum_{m=-l}^l Y^{lm}(\pi/2, \phi_0) \times \left[\mathcal{F}_{(-3)}^{\alpha l-3,m} + \mathcal{F}_{(-2)}^{\alpha l-2,m} + \mathcal{F}_{(-1)}^{\alpha l-1,m} + \mathcal{F}_{(0)}^{\alpha l,m} + \mathcal{F}_{(+1)}^{\alpha l+1,m} + \mathcal{F}_{(+2)}^{\alpha l+2,m} + \mathcal{F}_{(+3)}^{\alpha l+3,m} \right]. \quad (72)$$

$\mathcal{F}_{(j)}^{\alpha lm}$ are constructed from $\bar{h}^{(i)\ell m}$, $\bar{h}_{,r\pm}^{(i)\ell m}$, $\bar{h}_{,t}^{(i)\ell m}$ at $x^\mu = x_0^\mu$. The expressions for $\mathcal{F}_{(j)}^{\alpha lm}$ are quite lengthy and are explicitly given in appendix C of [32] for circular and in appendix C of [1] for eccentric orbits in Schwarzschild geometry. For this reason, we omit presenting them here. However, we would like to remark that $\mathcal{F}_{(j)}^{\alpha lm}$ contain coupling terms between tensor modes ℓ and scalar modes l . This is because the metric perturbation $\bar{h}_{\mu\nu}$ is decomposed in terms of *tensor* modes ℓ , but the GSF is computed by summing over *scalar* modes l (the regularization procedure requires the mode decomposition to be done in spherical harmonics [15], [18]). As a result, a given scalar spherical harmonic mode l will couple to 5 tensor spherical harmonic modes with $\ell - 2 \leq l \leq \ell + 2$ for the r -component, and to 7 tensor modes $\ell - 3 \leq l \leq \ell + 3$ for the t -component of $\mathcal{F}_{(j)}^{\alpha l}$. This is the reason why the index (j) in Eq.(72) goes from (-3) to (3) .

An extra simplification arises in Eq.(72) because the spherical harmonics $Y^{lm}(\pi/2, \phi_0) = 0$ for $l - m = \text{odd}$. Furthermore, because $\bar{h}^{(i)Y^{lm}} \rightarrow [\bar{h}^{(i)Y^{lm}}]^*$ under $m \rightarrow -m$, we compute the sum only from $m = 1$ to $m = \ell$ then fold over the m -sum properly to include the $m < 0$ contribution and finally add to these the $m = 0$ term in the summation in Eq.(72). This is then regularized at each l mode via Eq. (69).

To obtain the final value for the GSF, we compute the sum over all scalar l modes. Since the t -component converges exponentially, $l_{\text{max}} \approx 10$ suffices to obtain the value of $F^t(x_0)$ to machine accuracy. However, the r -component of the GSF falls off as $L_{1/2}^{-2}$ and this converges much more slowly. As we are using finite computer power to calculate an infinite sum over l , we must truncate the sum for the r -component at some $l = l_{\text{max}}$ (usually somewhere between 15 and 30) and use fitting methods to estimate contribution from the $l > l_{\text{max}}$ modes. This contribution accounts for at most $\sim 2\%$ to the overall GSF [32] and is called ‘‘the large- l tail’’. The details of how to compute it are given extensively in section III E of [32]. Basically, one extrapolates the $l > l_{\text{max}}$ terms in the sum using polynomial fits in powers of $L_{1/2}^{-2}$. As we use the same fitting method as [32], we refrain from elaborating any further. The details can be found there but let us discuss briefly how the tail error depends on the parameters used to do the fit.

There are two free parameters that determine the large- l tail. The first one is the number k of l modes $\in [l_{\text{max}} + 1 - k, l_{\text{max}}]$ that we select for the extrapolation. The second is N , which determines the degree of the polynomial fit in powers of $L_{1/2}^{-2}$. We use a numerical scheme that varies these two parameters (k, N) and finds the optimal values for both by comparing the error between the regularized l modes $F_{\text{reg}}^{r l_{\text{max}}+1-k \leq l \leq l_{\text{max}}}$ obtained from the fitting formula and the actual numerical values computed by solving the Einstein equations. Our scheme uses the following ranges for the two parameters: $2 \leq N \leq 6$ and $5 \leq k \leq 12$ depending on the total number of l modes that we compute (varies from 15 to 30). Because our frequency-domain code is able to compute up to 30 modes within an hour for $r_0 < 20M$, we are able to reduce the fractional error in the tail computation to $\sim 10^{-8}$. As we will see below, the uncertainty in the large- l tail is not always the source of the most significant error in our computation.

A. Summary of Methods and Computational Details

Working in the frequency domain, we started by numerically solving the 10 coupled field equations (13) for the radial fields $R_{\ell m}^{(i)}(r)$ (the modes $(\ell, m) = (0, 0), (\text{odd}, 0)$ have analytic solutions). To this end, for the first time, we calculated the boundary conditions for the radial fields in Lorenz gauge. We constructed linearly independent bases of homogeneous solutions and used these to obtain the inhomogeneous solutions $R_{\ell m}^{(i)}(r_0)$ and their $r \rightarrow r_0^\pm$ r -derivatives via junction conditions. Following the prescription of [32], we computed the $\mathcal{F}_{(j)}^{t lm \pm}, \mathcal{F}_{(j)}^{r lm \pm}$ of Eq. (72). The l modes of the ‘full’ GSF are then given by this equation. We regularized the GSF at each l mode with the help of Eq. (69) then added all the individual l -mode contributions together. Finally, for the r -component, we added the large- l tail to the l sum to account for the $F_{\text{reg}}^{r l > l_{\text{max}}}$ terms that we did not actually compute. It is this final result that equals the actual gravitational self-force. It is this quantity that we compare with BS in section V.

Our numerical code is written in C and uses Gnu Scientific Library (GSL) repositories [52] for the numerical integration of the ODEs and matrix algebra used in obtaining the inhomogeneous solutions. After exhaustive numerical experimentation, we selected to work with the Runge-Kutta Prince-Dormand (rk8pd) numerical integration routine as this proved to be the fastest. For our matrix inversion, we opted for the lower-upper (LU) triangular matrix decomposition. We use a single desktop machine with two quad-cores to run our code, which proved to be more than sufficient for GSF computations for circular orbits. More than 95% of the computing time is taken up by the numerical integration of the coupled ODEs. This task is further multiplied because of the need to construct N -dimensional bases of homogeneous solutions. For example, a GSF computation due to the first 15 scalar modes (i.e. tensor $\ell = 0 \dots 18$) numerically integrates various coupled ODEs a total of 2192 times.

The speed of the numerical ODE integrator depends on a few freely specifiable parameters: the size of the integration domain $[r_{in}^*, r_{out}^*]$, and the numerical accuracy thresholds $(\Delta_{rel}, \Delta_{abs})$ used by the integrator. Given an ODE, the code picks the smaller of the two thresholds to integrate. We have empirically determined that a relative ODE solver accuracy of $\Delta_{rel} = 10^{-10}$ is sufficient for computing the GSF to within an overall fractional error of $\lesssim 10^{-6}$ for runs with orbital radii $6M \leq r_0 \leq 50M$. However, for $r_0 > 50M$ runs, we observed that Δ_{rel} needs to be brought as close to machine accuracy as reliably possible i.e. 10^{-14} . This is because the transition region between the outer wave-zone (where the homogeneous fields $\bar{h}^{(i)} \rightarrow e^{-i\omega_m(t-r_*)}$) and the region where the fields exhibit power-law growth (near r_0) is farther out for larger r_0 . Therefore, the numerical solutions can possibly grow by more than 20 orders of magnitude as the routine integrates from r_{out} to r_0 . This fundamentally limits the accuracy that we can reach with a numerical integrator using double floating point precision. After some numerical experimentation, we settled on a scheme that adaptively varies $\Delta_{rel}, \Delta_{abs}$ with increasing r_0 . The scheme works well for up to $r_0 = 100M$ beyond which the accuracy thresholds thread very close to machine accuracy and the runtimes grow unreasonably long.

The runtimes are rather insensitive to the location of r_{in}^* . The reason is that the potential $V_{\ell m}$ is very ‘flat’ near the event horizon (less than 1% variance as one goes from $r_{in}^* = -35$ to -55), so the solutions hardly change. On the other hand, the runtimes do depend heavily on the location of r_{out}^* . Therefore, its location must be chosen carefully. We elaborate more on this in the next subsection.

B. The Error Budget

The major sources of error that go into our computation are: (1) Error in the large- l tail, (2) Error in the numerical matrix inversions used to construct the inhomogeneous solutions, (3) Numerical discretization error in the numerical integration of the ODEs, and (4) The fact that the boundary conditions are not computed at $r^* = \pm\infty$.

We determined that the error coming from the finiteness of the locations of the boundary points is much smaller than the other three sources of error. After some numerical experimentation, we came up with a satisfactory location for r_{out} (r_{out}^*) keeping in mind the wave-zone condition $r_{out} \gg \ell r_0 / \omega_m$ and the fact that our code slows down too much if r_{out} is unnecessarily too far out. This optimal choice was mentioned earlier in section III A. We tested the sensitivity of our solutions against changing r_{out} . We found that the relative variation in $|\bar{h}^{(i)}|$ was $\lesssim \mathcal{O}(10^{-12})$ when r_{out} was increased by up to one order of magnitude.

We have already commented on the errors in the large- l tail computation. Our usual standard has been a fractional error of 10^{-6} in the large- l tail. As mentioned in section IV, we can reduce this error to nearly 1.0×10^{-8} by computing more numerical modes, but this naturally increases the runtimes. On the other hand, if we adhere to a fractional error of 10^{-4} or 10^{-5} then we can reduce the overall runtimes considerably by computing less modes. We show this in Fig. 1, where we display plots of runtimes vs. r_0 for overall fractional errors of $10^{-4}, 10^{-6}$ and 10^{-7} . In short, we have a good understanding and good control over the uncertainty in the large- l tail.

The numerical discretization error coming from the numerical integration of the ODEs contributes much less to the overall error than the other error sources mentioned here. The GSL ODE integrator routines are very robust and have a very good handle on discretization errors. Our own numerical tests showed that these errors have magnitudes $\lesssim \mathcal{O}(10^{-12})$ with respect to the inhomogeneous fields.

Finally, as mentioned in section III B 1, the biggest source of error comes from the numerical inversion of the matrix constructed from the homogeneous solutions. This becomes the dominant source of error for $r_0 \gtrsim 50M$. An inspection of the matrix inversion output for each (ℓ, m) mode reveals that the inversion errors grow with increasing $\ell - m$ and that they are also larger in the even parity sector. We monitored the condition numbers of the matrices and found out that for even parity modes with $\ell - m > 15$, they routinely exceeded 10^{12} for $r_0 > 50M$ and got as large as 10^{22} for $r_0 > 100M$. Further inspection of these large ℓ , large r_0 even modes revealed that the determinant threads very close to zero. This is an indication that our linearly independent bases of homogeneous solutions start becoming degenerate in this region. The reason why this happens for large $\ell - m$ is due to particular way we have formulated the location of the outer boundary by setting $r_{out} = 50 \ell r_0 / \omega_m = 50 r_0^{5/2} (\ell / m)$. From this, one sees that r_{out} reaches its maximum value when $\ell - m$ reaches its maximum value. So, this ‘degeneracy problem’ is actually caused by large

values for r_{out} . What happens is that because the leading order power-law for each homogeneous field dominates near r_0 , the solutions that have the same power-law behavior start looking numerically identical as the integrator works its way in toward r_0 . As we look at the values of the fields for larger r_0 runs, the matrices constructed from the even parity homogeneous fields become linearly dependent (singular valued). This means the matrix inversion is not very reliable. We find that this degeneracy of even parity solutions becomes significant for the runs where $r_0 \gtrsim 50M$. So, any numerical ODE integration that routinely goes beyond this point ($r_0 \approx 50M$) starts running into this degeneracy problem.

We model the error coming from the singular-valuedness of the matrices as a continuity violation in the inhomogeneous fields $R^{(i)}(r)$ at $r = r_0$. This continuity violation, $\Delta^{(i)}$, is most prominent for the fields $R^{(2),(4),(5)}$ where it is about $\mathcal{O}(10^4)$ larger than the violations in the other fields. In the worst case, e.g. $r_0 = 150M$ and $\ell = 17$, $m = 1$; $\Delta^{(5)} \approx 10^{-5}$. However, even at $r_0 = 150M$, the violation quickly subsides to $\lesssim 10^{-9}$ once $m \geq 2$ whatever ℓ may be, but because the GSF is constructed by summing over all (ℓ, m) modes, this error is additive. For a computation of the GSF requiring $\ell_{\text{max}} = 18$, the relative strength of the error is amplified by a factor of $\sim 10^2 - 10^3$ going from from a single mode to the final GSF, which is constructed from the sum of $\mathcal{O}(10^2)$ modes. This is indeed what we observe numerically. We have not yet looked into fixing this inversion problem but we are aware that using singular-valued decompositions for the matrices do not offer an improvement [53]. Be that as it may, we do not think this to be a problem for when we compute the GSF for eccentric orbits because we will be mostly interested in the strong field regime of $r_0 < 20M$. However, for equatorial eccentric orbits in frequency domain, we expect to encounter a similar type of degeneracy in our solutions due to the fact that the frequency spectrum is determined by two fundamental frequencies: $\omega_{mn} = m\Omega_\phi + n\Omega_r$. There will be points in the parameter space where the two terms in ω_{mn} will conspire to cancel each other to values less than 10^{-4} . When this happens, the conditions numbers for matrices of homogeneous solutions grow to values that render the matrix inversion unreliable. We are currently working on a solution to this problem.

V. RESULTS

We present the output of our frequency-domain code for the gravitational self-force in Tables 2 and 3. For comparison, we include the results of BS [32] and the relative difference between our respective values for the t -, and r -components of the GSF. We find very good agreement with the results of BS (within their error bars) for r_0 up to $\sim 100M$. However, beyond that, our values stray from theirs. Given that Berndtson [35] agrees with BS within their quoted errors bars for up to $150M$, we must conclude that the degeneracy problem renders our results unreliable beyond $r_0 \sim 100M$. However, as our results show, in the strong field regime our f-domain results are much more accurate than their time-domain counterparts.

As another way of confirming our results and determining the magnitude of the error in our GSF computation, we computed the energy flux of the gravitational waves leaving the system and compared the value of the total radiated power with the total rate of energy loss given by the dissipative component of the GSF. In the case of circular orbits, only the t -component of the GSF is dissipative so the rate of energy loss can be related to F^t as follows:

$$\frac{d\tilde{E}_0}{d\tau} = -\mu^{-1}F_t. \quad (73)$$

In terms of Schwarzschild time t , this becomes $d\tilde{E}_0/dt = -(\mu u_0^t)^{-1}F_t$, where u_0^t is the t -component of the 4-velocity of the particle evaluated at $r = r_0$. In the adiabatic approximation, where $\mu/M \ll 1$, $d\tilde{E}_0/dt$ can be taken to be the average rate of energy loss per orbit. Energy conservation dictates that this loss of energy must be balanced by the total energy flux carried by gravitational waves radiated out to infinity and absorbed into the black hole. Therefore, we have the following balance equation:

$$\dot{E}_{\text{total}} \equiv \dot{E}_\infty + \dot{E}_{\text{EH}} = -\mu \frac{d\tilde{E}_0}{dt} = F_t/u_0^t, \quad (74)$$

where the overdot now denotes d/dt and $\dot{E}_\infty, \dot{E}_{\text{EH}}$ denote the gravitational wave flux radiated to infinity and through the event horizon (EH), respectively. These fluxes are constructed from the metric fields $\bar{h}^{(i)\ell m}$. We omit the details of this construction here, but for the interested reader they can be found in [32, 54, 55]. Let us simply display the final expressions for the fluxes:

$$\dot{E}_\infty = \sum_{\ell=2}^{\infty} \sum_{m=-\ell}^{\ell} \frac{\mu^2 m^2 \Omega_0^2}{64\pi\lambda\ell(\ell+1)} \left| \bar{h}_\infty^{(\ell)} - i\bar{h}_\infty^{(10)} \right|^2, \quad (75)$$

$$\begin{aligned} \dot{E}_{\text{EH}} = & \sum_{\ell=2}^{\infty} \sum_{m=-\ell}^{\ell} \frac{\mu^2 \lambda \ell(\ell+1)}{256\pi M^2 (1 + 16M^2 m^2 \Omega_0^2)} \\ & \times \left| \bar{h}_{\text{EH}}^{(1)} + \frac{1 + 4iMm\Omega_0}{\ell(\ell+1)} \left[\bar{h}_{\text{EH}}^{(5)} - i\bar{h}_{\text{EH}}^{(9)} + 2iMm\Omega_0 \lambda^{-1} \left(\bar{h}_{\text{EH}}^{(7)} - i\bar{h}_{\text{EH}}^{(10)} \right) \right] \right|^2, \end{aligned} \quad (76)$$

where $\bar{h}_{\infty, \text{EH}}^{(i)}$ implies that the metric field is to be evaluated (in frequency domain) at $r = \infty, 2M$, respectively. Using Eqs. (75), (76) and our results for F^t , we compute the total radiated power \dot{E}_{total} and compare the resulting values. The relative difference between the two results is shown in the last column of Table 3, which shows that the agreement is excellent for small r_0 . It naturally gets worse for increasing values of r_0 . We also found that the disagreement between the two values for \dot{E}_{total} matched our overall fractional error in F^t well.

We also present the runtimes for our code for three different relative accuracies. These are quantified by the overall fractional error in our numerical computation of the GSF. We have selected to present results for overall fractional errors of $10^{-4}, 10^{-6}, 10^{-7}$. We display the runtimes for these in Fig. 1. As can be seen from the upper left panel of the figure, at a relative accuracy of 10^{-4} , our code takes less than two minutes to compute the GSF for radii less than $\sim 15M$. This grows nearly to a day as r_0 approaches $100M$. Although toward $100M$ the runtimes appear to level off, this is due to our logarithmic scale for the vertical axis. The runtimes increase by ~ 100 minutes in going from $70M$ to $80M$, and $80M$ to $90M$. In the same figure, upper right panel, one sees that demanding an accuracy of 10^{-6} increases the runtimes by a factor of two to three for $r_0 \lesssim 10M$. However, beyond $r_0 = 50M$, this accuracy becomes unattainable. Finally, we find it quite difficult to keep the overall fractional error less than 10^{-7} . But as the lower left panel of the figure shows, an accuracy standard of 10^{-7} is achievable for $r_0 \lesssim 30M$ and the overall runtimes are not prolonged by much for these strong field GSF computations. Interestingly enough, in the regime $r_0 \lesssim 20M$, the $r_0 \leq 8M$ runs seem to take more time than $r_0 \geq 9M$ runs. This was artificially caused by our need to compute more modes in order to lower the error in the large- l tail for the $r_0 \leq 8M$ runs. It turns out that for the smallest radii, the large- l tail can not be computed to the desired accuracy of 10^{-6} or 10^{-7} using just 15 or 17 scalar modes, which is what we had done for the $r_0 \geq 9M$ runs. We think the reason for this is that the magnitudes of the individual l modes of the GSF are large enough for $r_0 \leq 8M$ that more modes are needed in order for the tail to be fit correctly. Finally, in the lower right panel, we present the computation times for a given $r_0 \leq 20M$ run for all three accuracies. As expected, the runtimes increase with demand for higher accuracy. However, by how much they increase is not the same at each radius. There is also the anomalous data point for the $10M$ run where the 10^{-7} accuracy computation takes slightly less time than the 10^{-6} one. This comes from our not having explored thoroughly enough the free parameters that determine the overall error and runtime such as l_{max} , number of points used in the tail and the numerical ODE integrator accuracy thresholds. Most importantly, the figure shows that all $r_0 \leq 20M$ runs take less than 15 minutes up to an accuracy of 10^{-7} .

It should also be added that even on our modest desktop, we can simultaneously perform a dozen strong field runs without significantly affecting individual runtimes. For example, in a 15 minute period, we can compute the GSF for all integer orbital radii from $6M$ to $10M$ to an accuracy of 10^{-6} . We find the speed of our code to be fast enough to encourage continuing this frequency-domain approach to tackle the eccentric Schwarzschild problem for the GSF. Work is currently underway and the preliminary results are encouraging. We intend to apply these methods to the full Kerr problem later on.

VI. ACKNOWLEDGEMENTS

SA thanks Leor Barack, Nori Sago and Niels Warburton. This work was supported by STFC grant No. PP/E001025/1.

Appendix A: The Recursion Relations for The Boundary Conditions

1. Generic Odd and Even Modes

Recall that by *generic*, we mean the non-static ($m \neq 0$), $\ell > 1$ modes. Here, ω denotes $\omega_m = m\Omega_0$ and $L \equiv \ell(\ell+1)$. We begin by redisplaying the recursion relations for the outer boundary conditions (BC) for odd parity homogeneous

r_0/M	$(M/\mu)^2 F^r$	$(M/\mu)^2 F_{BS}^r$	Rel. diff.
6.0	$2.4466495(4) \times 10^{-2}$	2.44661×10^{-2}	4.0×10^{-6}
7.0	$2.149907776(8) \times 10^{-2}$	2.14989×10^{-2}	8.3×10^{-6}
8.0	$1.8357830(4) \times 10^{-2}$	1.83577×10^{-2}	7.1×10^{-6}
9.0	$1.5637099(1) \times 10^{-2}$	1.56369×10^{-2}	1.3×10^{-5}
10.0	$1.3389470(2) \times 10^{-2}$	1.33895×10^{-2}	2.2×10^{-6}
11.0	$1.155174593(6) \times 10^{-2}$	1.15518×10^{-2}	4.7×10^{-6}
12.0	$1.00462381(8) \times 10^{-2}$	1.00463×10^{-2}	6.2×10^{-6}
13.0	$8.8048853(3) \times 10^{-3}$	8.80489×10^{-3}	5.3×10^{-7}
14.0	$7.7730602(4) \times 10^{-3}$	7.77307×10^{-3}	1.3×10^{-6}
15.0	$6.9081719(3) \times 10^{-3}$	6.90815×10^{-3}	9.7×10^{-5}
20.0	$4.1570550(2) \times 10^{-3}$	4.15706×10^{-3}	1.2×10^{-6}
30.0	$1.9698169(3) \times 10^{-3}$	1.96982×10^{-3}	1.6×10^{-6}
40.0	$1.142883(1) \times 10^{-3}$	1.14288×10^{-3}	2.6×10^{-6}
50.0	$7.449480(1) \times 10^{-4}$	7.44949×10^{-4}	1.3×10^{-6}
60.0	$5.236083(3) \times 10^{-4}$	5.23613×10^{-4}	9.0×10^{-6}
70.0	$3.8801(1) \times 10^{-4}$	3.88010×10^{-4}	2.6×10^{-6}
80.0	$2.9896(1) \times 10^{-4}$	2.98979×10^{-4}	6.4×10^{-5}
90.0	$2.3739(1) \times 10^{-4}$	2.37406×10^{-4}	6.7×10^{-5}
100.0	$1.9304(1) \times 10^{-4}$	1.93063×10^{-4}	1.2×10^{-4}
120.0	$1.3483(1) \times 10^{-4}$	1.34868×10^{-4}	2.8×10^{-4}
150.0	$8.673(1) \times 10^{-5}$	8.68274×10^{-5}	1.1×10^{-3}

TABLE II: Output for the r -component of the gravitational self-force for various orbital radii r_0 compared with results of BS [32]. Column 2 contains our results; the number in parentheses indicates the size of the uncertainty in the last significant digit, e.g. $2.4466495(4) = 2.4466495 \pm 4 \times 10^{-7}$. In column 3, we display the results of BS for comparison. Column 4 gives the relative difference between our values and BS'. Our results are within their quoted error bars for nearly up to $r_0 = 100M$. Beyond that the disagreement seems to grow up $\mathcal{O}(10^{-3})$. Given that Berndtson's results [35] agree with BS better for large r_0 , we conclude that our current results are not reliable beyond $r_0 \approx 100M$. Nevertheless, as can be seen from the number of significant digits that we have included for F^r for $r_0 \lesssim 50M$, the frequency-domain results are much more accurate than time domain in the strong field regime.

fields R_9^\pm and R_{10}^\pm :

$$2i\omega k a_k^9 = C_{k-1} a_{k-1}^9 + D_{k-2} a_{k-2}^9 + E_{k-3} a_{k-3}^9 + 2a_{k-1}^{10} - 10M a_{k-2}^{10} + 12M^2 a_{k-3}^{10}, \quad (\text{A1})$$

$$2i\omega k a_k^{10} = I_{k-1} a_{k-1}^{10} + J_{k-2} a_{k-2}^{10} + K_{k-3} a_{k-3}^{10} + 2\lambda a_{k-1}^9 - 4M\lambda a_{k-2}^9, \quad (\text{A2})$$

where

$$\begin{aligned} C_k &= 4M i\omega k + k(k+1) - L - 4, & I_k &= 4M i\omega k + k(k+1) - L + 2, \\ D_k &= -6Mk - 4Mk^2 + 24M + 2ML, & J_k &= -6Mk - 4Mk^2 - 6M + 2ML, \\ E_k &= 4M^2(k^2 + 2k - 8), & K_k &= 4M^2(k^2 + 2k + 1). \end{aligned}$$

Next, we present the recursion relations for the inner BC

$$4M^2 k(k - 4M i\omega) b_k^9 = \tilde{C}_{k-1} b_{k-1}^9 + \tilde{D}_{k-2} b_{k-2}^9 + \tilde{E}_{k-3} b_{k-3}^9 + 2M b_{k-1}^{10} - 2b_{k-2}^{10}, \quad (\text{A3})$$

$$4M^2 k(k - 4M i\omega) b_k^{10} = \tilde{H}_{k-1} b_{k-1}^{10} + \tilde{J}_{k-2} b_{k-2}^{10} + \tilde{E}_{k-3} b_{k-3}^{10} - 4M\lambda b_{k-1}^9 - 2\lambda b_{k-2}^9 \quad (\text{A4})$$

$$(\text{A5})$$

where

$$\begin{aligned} \tilde{C}_k &= 2M(k + 12M i\omega k - 2k^2 + L - 4), & \tilde{H}_k &= 2M(k + 12M i\omega k - 2k^2 + L - 1), \\ \tilde{D}_k &= 4 + 12M i\omega k + L - k(k-1), & \tilde{J}_k &= -2 + 12M i\omega k + L - k(k-1), \\ \tilde{E}_k &= 2i\omega k. \end{aligned}$$

r_0/M	$(M/\mu)^2 F^t$	$(M/\mu)^2 F_{BS}^t$	Rel. diff.	$(M/\mu)^2 \dot{E}_{total}$	$(M/\mu)^2 F_t/u_0^t$	Rel. diff.
6.0	$-1.9947610064(3) \times 10^{-3}$	-1.99476×10^{-3}	5.0×10^{-7}	$9.4033935631 \times 10^{-4}$	$9.4033935626 \times 10^{-4}$	5.7×10^{-10}
7.0	$-7.411127850(9) \times 10^{-4}$	-7.41101×10^{-4}	1.2×10^{-5}	$4.001632906 \times 10^{-4}$	$4.001632909 \times 10^{-4}$	6.6×10^{-11}
8.0	$-3.307397510(3) \times 10^{-4}$	-3.30740×10^{-4}	1.2×10^{-5}	$1.9610454858 \times 10^{-4}$	$1.9610454864 \times 10^{-4}$	3.0×10^{-10}
9.0	$-1.668101230(4) \times 10^{-4}$	-1.66810×10^{-4}	1.2×10^{-5}	$1.0593325177 \times 10^{-4}$	$1.0593325178 \times 10^{-4}$	8.8×10^{-11}
10.0	$-9.19075772(7) \times 10^{-5}$	-9.19067×10^{-5}	1.0×10^{-5}	$6.151631678 \times 10^{-5}$	$6.151631677 \times 10^{-5}$	2.2×10^{-10}
11.0	$-5.41623002(6) \times 10^{-5}$	-5.41605×10^{-5}	1.2×10^{-5}	$3.779162580 \times 10^{-5}$	$3.771962578 \times 10^{-5}$	4.8×10^{-10}
12.0	$-3.3659568(1) \times 10^{-5}$	-3.36587×10^{-5}	1.2×10^{-5}	$2.42917009 \times 10^{-5}$	$2.42917010 \times 10^{-5}$	3.2×10^{-9}
13.0	$-2.1839249(2) \times 10^{-5}$	-2.18388×10^{-5}	1.2×10^{-5}	$1.620747493 \times 10^{-5}$	$1.620747489 \times 10^{-5}$	2.8×10^{-9}
14.0	$-1.4685410(2) \times 10^{-5}$	-1.46851×10^{-5}	1.2×10^{-5}	$1.115762106 \times 10^{-5}$	$1.115762104 \times 10^{-5}$	2.2×10^{-9}
15.0	$-1.0177145(1) \times 10^{-5}$	-1.01772×10^{-4}	1.2×10^{-5}	$7.88902019 \times 10^{-6}$	$7.88902015 \times 10^{-6}$	5.3×10^{-9}
20.0	$-2.2554391(2) \times 10^{-6}$	-2.25549×10^{-6}	2.2×10^{-5}	$1.87147091 \times 10^{-6}$	$1.87147088 \times 10^{-6}$	1.6×10^{-8}
30.0	$-2.8081894(8) \times 10^{-7}$	-2.80813×10^{-7}	2.1×10^{-5}	2.486484×10^{-7}	2.486486×10^{-7}	1.1×10^{-6}
40.0	$-6.51228(2) \times 10^{-8}$	-6.51219×10^{-8}	1.5×10^{-5}	5.95014×10^{-8}	5.95015×10^{-8}	2.9×10^{-6}
50.0	$-2.108456(4) \times 10^{-8}$	-2.10849×10^{-8}	3.0×10^{-5}	1.962458×10^{-8}	1.962453×10^{-8}	2.3×10^{-6}
60.0	$-8.41300(3) \times 10^{-9}$	-8.41306×10^{-9}	7.0×10^{-6}	7.92644×10^{-9}	7.92641×10^{-9}	3.9×10^{-6}
70.0	$-3.8743(1) \times 10^{-9}$	-3.87411×10^{-9}	4.1×10^{-5}	3.6819×10^{-9}	3.6818×10^{-9}	3.5×10^{-5}
80.0	$-1.9804(1) \times 10^{-9}$	-1.98069×10^{-9}	4.6×10^{-5}	1.8945×10^{-9}	1.8946×10^{-9}	4.2×10^{-5}
90.0	$-1.0966(3) \times 10^{-9}$	-1.09654×10^{-9}	9.1×10^{-5}	1.0541×10^{-9}	1.0544×10^{-9}	2.6×10^{-4}
100.0	$-6.464(2) \times 10^{-10}$	-6.46305×10^{-9}	2.1×10^{-4}	6.238×10^{-10}	6.240×10^{-10}	3.2×10^{-4}
120.0	$-2.596(9) \times 10^{-10}$	-2.59096×10^{-10}	1.9×10^{-3}	2.516×10^{-10}	2.525×10^{-10}	3.6×10^{-3}
150.0	$-8.44(6) \times 10^{-11}$	-8.47172×10^{-11}	3.4×10^{-3}	8.27×10^{-11}	8.22×10^{-11}	6.1×10^{-3}

TABLE III: Output for the t -component of the gravitational self-force for various radii r_0 . Our results are in column 2. In column 3, we show the results of BS for F^t and display the relative difference in column 4. Once again, our results fall within BS' error bars for $r_0 \lesssim 100M$ and again the error increases up to $\mathcal{O}(10^{-3})$ for $r_0 = 150M$. And as was the case with F^r , our frequency-domain results for F^t also have much smaller uncertainties in the $r_0 \lesssim 50M$ regime compared with those of BS. We also checked our results for F^t using energy balance arguments. Since only the t -component of the GSF is dissipative for circular orbits, it can be related to the energy flux leaving the system as we have outlined in section V. The total energy flux is computed using the two different methods and these results are displayed in columns 5 and 6 down to the significant digit at which they start disagreeing. Column 7 contains the relative difference between the two values. Once again, the agreement is extremely good for small r_0 and grows to $\mathcal{O}(10^{-3})$ as r_0 increases to $150M$.

Now, we turn our attention to the BC for the even parity fields $R_{1,3,5,6,7}^\pm$. We start with the recursion relations for the outer BC for R_1^\pm, R_3^\pm and R_6^\pm :

$$2i\omega k a_k^1 = C_{k-1}^1 a_{k-1}^1 + (2 - 4Mi\omega) a_{k-1}^3 + 2a_{k-1}^5 + 2a_{k-1}^6 + D_{k-2}^1 a_{k-2}^1 + D_{k-2}^3 a_{k-2}^3 - 12M a_{k-2}^5 - 20M a_{k-2}^6 + E_{k-3}^1 a_{k-3}^1 + E_{k-3}^3 a_{k-3}^3 + 16M^2 a_{k-3}^5 + 56M^2 a_{k-3}^6 + F_{k-4}^3 a_{k-4}^3 - 48M^3 a_{k-4}^6, \quad (\text{A6})$$

$$2i\omega k a_k^3 = C_{k-1}^1 a_{k-1}^3 + 2(a_{k-1}^1 - a_{k-1}^5 - a_{k-1}^6) + D_{k-2}^1 a_{k-2}^3 + 4M(-a_{k-2}^1 + a_{k-2}^5 + 3a_{k-2}^6) + E_{k-3}^1 a_{k-3}^3 - 16M^2 a_{k-3}^6, \quad (\text{A7})$$

$$2i\omega k a_k^6 = C_{k-1}^1 a_{k-1}^6 + 2(a_{k-1}^1 - a_{k-1}^5 - a_{k-1}^3) + D_{k-2}^1 a_{k-2}^6 + 4M(-a_{k-2}^1 + a_{k-2}^5 + 3a_{k-2}^3) + E_{k-3}^1 a_{k-3}^6 - 16M^2 a_{k-3}^3, \quad (\text{A8})$$

where

$$C_k^1 = k(k+1) + 4Mi\omega k - 2 - L, \quad (\text{A9})$$

$$D_k^1 = 2M(5 + L - 2k^2 - 3k), \quad D_k^3 = 2M(2k - 8 + 4Mi\omega), \quad (\text{A10})$$

$$E_k^1 = 4M^2(k^2 + 2k - 3), \quad E_k^3 = 8M^2(5 - 2k), \quad F_k^3 = 16M^3(k - 2). \quad (\text{A11})$$

For the field R_5^\pm , we have:

$$2i\omega k a_k^5 = C_{k-1}^5 a_{k-1}^5 + 2L(a_{k-1}^1 - a_{k-1}^3 - a_{k-1}^6) + 2a_{k-1}^7 + D_{k-2}^5 a_{k-2}^5 - 10M a_{k-2}^7 + 2ML(-2a_{k-2}^1 + 4a_{k-2}^3 + 5a_{k-2}^6) + E_{k-3}^5 a_{k-3}^5 + 4M^2(-2La_{k-3}^3 - 3La_{k-3}^6 + 3a_{k-3}^7), \quad (\text{A12})$$

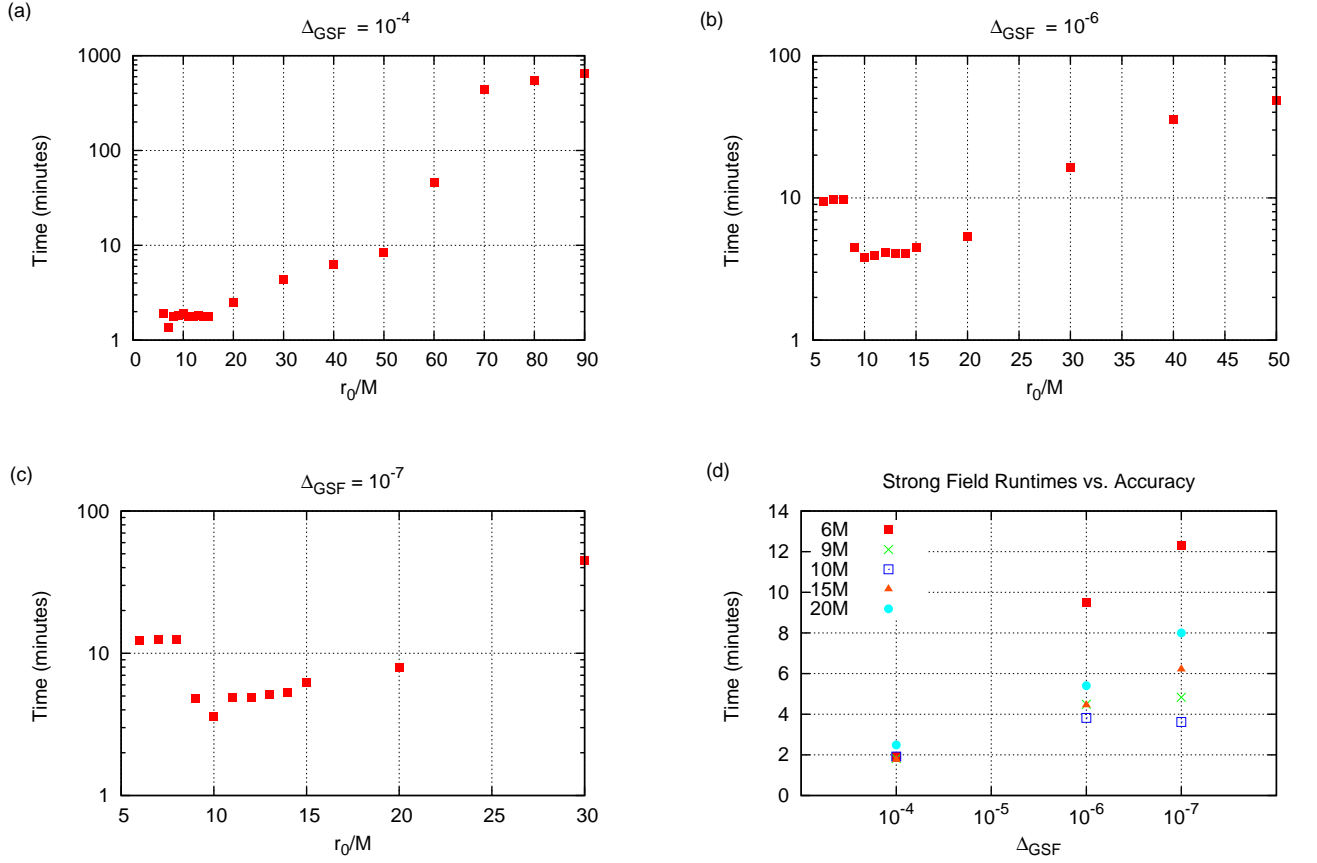


FIG. 1: The runtimes for the 10^{-4} , 10^{-6} , 10^{-7} overall fractional error runs. Panels (a), (b) and (c) display plots of runtime (in minutes) versus orbital radius r_0 at which we compute the GSF. Δ_{GSF} denotes the overall fractional error in our numerical computation of the GSF. This error is what we refer to as our (relative) ‘accuracy’. As can be seen in panel (a), at an accuracy of 10^{-4} , our code takes less than two minutes to compute the GSF for $r_0 \lesssim 15M$. This grows nearly to a day as r_0 approaches $100M$. Panel (b) shows that an accuracy of 10^{-6} increases the runtimes by a factor of two to three for $r_0 \lesssim 10M$, but the runtimes are still $\lesssim 10$ minutes for $r_0 \lesssim 20M$. However, beyond $r_0 = 50M$, this accuracy becomes unattainable. As panel (c) shows, an accuracy of 10^{-7} is achievable for $r_0 \lesssim 30M$ and the overall runtimes do not change much for these strong field GSF computations. Interestingly enough, for $r_0 \lesssim 20M$, the $r_0 \leq 8M$ runs seem to take more time than $r_0 \geq 9M$ runs. This is a result of our having to compute more modes to obtain the GSF for the $r_0 \leq 8M$ runs because the large- l tail could not be computed to the desired accuracy of 10^{-6} or 10^{-7} using just 17 scalar modes, which is what we had done for the $r_0 \geq 9M$ runs. We think the reason for this is that the magnitudes of the individual l modes of the GSF are large enough for $r_0 \leq 8M$ that more modes are needed in order for the tail to be fit correctly. Finally in panel (d), we present the runtimes for a few $r_0 \leq 20M$ run for all three accuracies. As expected, the runtimes increase with demand for higher accuracy (except for the $10M$ run). Most importantly, the figure shows that all $r_0 \leq 20M$ runs take less than 15 minutes up to an accuracy of 10^{-7} .

where

$$C_k^5 = k(k+1) + 4Mi\omega k - 4 - L, \quad D_k^5 = 2M(12 - 2k^2 - 3k + L), \quad (\text{A13})$$

$$E_k^5 = 4M^2(k^2 + 2k - 8). \quad (\text{A14})$$

And for R_7^\pm :

$$2i\omega k a_k^7 = C_{k-1}^7 a_{k-1}^7 + 2\lambda a_{k-1}^5 + D_{k-2}^7 a_{k-2}^7 - 4M\lambda a_{k-2}^5 + E_{k-3}^7 a_{k-3}^7, \quad (\text{A15})$$

where

$$C_k^7 = k(k+1) + 4Mi\omega k - L + 2, \quad D_k^7 = 2M(L - 3 - 2k^2 - 3k), \quad (\text{A16})$$

$$E_k^7 = 4M^2(k^2 + 2k + 1). \quad (\text{A17})$$

Next, we present the recursion relations for the inner boundary conditions for the same fields in the same order. We start with:

$$8M^3k(4Mi\omega - k)b_k^1 = \tilde{C}_{k-1}^1 b_{k-1}^1 + \tilde{C}_{k-1}^3 b_{k-1}^3 - 8M^2 b_{k-1}^5 + \tilde{D}_{k-2}^1 b_{k-2}^1 + \tilde{D}_{k-2}^3 b_{k-2}^3 - 8M b_{k-2}^6 + \tilde{E}_{k-3}^1 b_{k-3}^1 + 2(1 + 2Mi\omega) b_{k-3}^3 + 2b_{k-3}^5 + 2b_{k-3}^6 - \tilde{F}_{k-4}^1 b_{k-4}^1, \quad (\text{A18})$$

where

$$\tilde{C}_k^1 = 4M^2(1 + 3k^2 - L - 16Mi\omega k - k), \quad \tilde{C}_k^3 = 8M^2(2Mi\omega - k), \quad (\text{A19})$$

$$\tilde{D}_k^1 = 2M(3k^2 - 2k - 2L - 1 - 24Mi\omega k), \quad \tilde{D}_k^3 = 4M(4Mi\omega - k - 1), \quad (\text{A20})$$

$$\tilde{E}_k^1 = k(k-1) - 16Mi\omega k - 2 - L, \quad \tilde{F}_k^1 = 2i\omega k. \quad (\text{A21})$$

$$4M^2k(4Mi\omega - k)b_k^3 = \tilde{G}_{k-1}^3 b_{k-1}^3 + 4M(b_{k-1}^1 - b_{k-1}^5 + b_{k-1}^6) + \tilde{H}_{k-2}^3 b_{k-2}^3 + 2(b_{k-2}^1 - b_{k-2}^5 - b_{k-2}^6) - \tilde{F}_{k-3}^1 b_{k-3}^3, \quad (\text{A22})$$

$$4M^2k(4Mi\omega - k)b_k^6 = \tilde{G}_{k-1}^3 b_{k-3}^6 + 4M(b_{k-1}^1 - b_{k-1}^5 + b_{k-1}^3) + \tilde{H}_{k-2}^3 b_{k-2}^6 + 2(b_{k-2}^1 - b_{k-2}^5 - b_{k-2}^3) - \tilde{F}_{k-3}^1 b_{k-3}^6, \quad (\text{A23})$$

where

$$\tilde{G}_k^3 = 2M(2k^2 - k - L + 1 - 12Mi\omega k), \quad (\text{A24})$$

$$\tilde{H}_k^3 = k(k-1) - L - 2 - 12Mi\omega k. \quad (\text{A25})$$

$$4M^2k(4Mi\omega - k)b_k^5 = \tilde{I}_{k-1}^5 b_{k-1}^5 + 2ML(2b_{k-1}^1 + b_{k-1}^6) - 2Mb_{k-1}^7 + \tilde{J}_{k-2}^5 b_{k-2}^5 + 2L(b_{k-2}^1 - b_{k-2}^3 - b_{k-2}^6) + 2b_{k-2}^7 - \tilde{F}_{k-3}^1 b_{k-3}^5, \quad (\text{A26})$$

where

$$\tilde{I}_k^5 = 2M(2k^2 - k - L + 4 - 12Mi\omega k), \quad (\text{A27})$$

$$\tilde{J}_k^5 = k(k-1) - L - 4 - 12Mi\omega k. \quad (\text{A28})$$

And, finally

$$4M^2k(4Mi\omega - k)b_k^7 = \tilde{G}_{k-1}^3 b_{k-1}^7 + 4M\lambda b_{k-1}^5 + \tilde{K}_{k-2}^7 b_{k-2}^7 + 2\lambda b_{k-2}^5 - \tilde{F}_{k-3}^1 b_{k-3}^7, \quad (\text{A29})$$

where

$$\tilde{K}_k^7 = k(k-1) - L + 2 - 12Mi\omega k. \quad (\text{A30})$$

2. The Even Dipole ($\ell = 1, m = 1$) Mode

The recursion relations for $a_k^{1,3,6}, b_k^{1,3,6}$ do not change. However, we end up with new recursion relations for the inner and outer boundary conditions for R_5^\pm

$$4M^2k(4Mi\omega - k)b_k^5 = \tilde{I}_{k-1}^5 b_{k-1}^5 + 2ML(2b_{k-1}^1 + b_{k-1}^6) - 2Mb_{k-1}^7 + \tilde{J}_{k-2}^5 b_{k-2}^5 + 2L(b_{k-2}^1 - b_{k-2}^3 - b_{k-2}^6) + 2b_{k-2}^7 - \tilde{F}_{k-3}^1 b_{k-3}^5, \quad (\text{A31})$$

$$2i\omega k a_k^5 = C_{k-1}^5 a_{k-1}^5 + 2L(a_{k-1}^1 - a_{k-1}^3 - a_{k-1}^6) + 2a_{k-1}^7 + D_{k-2}^5 a_{k-2}^5 - 10M a_{k-2}^7 + 2ML(-2a_{k-2}^1 + 4a_{k-2}^3 + 5a_{k-2}^6) + E_{k-3}^5 a_{k-3}^5 + 4M^2(-2La_{k-3}^3 - 3La_{k-3}^6 + 3a_{k-3}^7), \quad (\text{A32})$$

where $\omega = m\Omega_0$ and $L \equiv \ell(\ell + 1)$ as before. The coefficients $C_k^5, D_k^5, E_k^5, \tilde{F}_k^1, \tilde{I}_k^5, \tilde{J}_k^5$ are the same as before, displayed in Eqs. (A13), (A14), (A21), (A27) and (A28).

3. The Static ($m = 0$) Even Modes

Recall that because we are now dealing with static modes, we no longer have in or outgoing waves at the boundaries. For the inner BC, we use the following ansatz:

$$R_i^- = \sum_{k=k_{\text{start}}}^{\infty} b_k^i (r - 2M)^k, \quad (\text{A33})$$

where we now have three fields labelled by $i = 1, 3, 5$. New recursion relations for the inner BC are:

$$8M^3 k(k-2)b_k^1 = \bar{F}_{k-1}^1 b_{k-1}^1 + \bar{G}_{k-2}^1 b_{k-2}^1 + \bar{G}_{k-2}^3 b_{k-2}^3 - 2M b_{k-2}^5 \\ + \bar{E}_{k-3}^1 b_{k-3}^1 + \bar{E}_{k-3}^3 b_{k-3}^3 - b_{k-3}^5, \quad (\text{A34})$$

$$4Mk(k-1)b_k^5 = \bar{C}_{k-1}^5 b_{k-1}^5 - 4MLb_{k-1}^1 + \bar{D}_{k-2}^5 b_{k-2}^5 + 2L(b_{k-2}^3 - b_{k-2}^1), \\ \bar{C}_{k-1}^3 b_{k-1}^3 = \bar{C}_{k-1}^1 b_{k-1}^1 - 8M^3 k b_k^1 + 4M^2 b_{k-1}^5 + \bar{D}_{k-2}^3 b_{k-2}^3 + \bar{D}_{k-2}^1 b_{k-2}^1 \\ + 4M b_{k-2}^5 + \bar{E}_{k-3}^3 b_{k-3}^3 + \bar{E}_{k-3}^1 b_{k-3}^1 + b_{k-3}^5, \quad (\text{A35})$$

where

$$\bar{C}_k^1 = -4M^2(k+1), \quad \bar{C}_k^3 = 4M^2 k(k-1), \quad \bar{C}_k^5 = 2ML - 4M(1+k^2), \quad (\text{A36})$$

$$\bar{D}_k^1 = 2M(k-2), \quad \bar{D}_k^3 = 2M(L+k(1-2k)), \quad \bar{D}_k^5 = L - k(k+1), \quad (\text{A37})$$

$$\bar{E}_k^1 = L+1-k^2, \quad \bar{E}_k^3 = k-1, \quad \bar{G}_k^3 = 2Mk, \quad (\text{A38})$$

$$\bar{F}_k^1 = 4M^2(L+1+4k-3k^2), \quad \bar{G}_k^1 = 2M(2L+2+2k-3k^2). \quad (\text{A39})$$

For the outer boundary conditions, we make the following ansatz:

$$R_i^+ = \sum_{k=k_{\text{start}}}^{\infty} \frac{a_k^i + \bar{a}_k^i \ln r}{r^k}. \quad (\text{A40})$$

Recall that the recursion relations for $a_k^1, a_k^3, a_k^5, \bar{a}_k^1, \bar{a}_k^3, \bar{a}_k^5$ are determined by the three free parameters $a_\ell^3, a_\ell^5, a_{\ell+2}^5$. We now present these relations in their coupled form:

$$\hat{C}_k^1 a_k^1 = (k+1)a_k^3 + a_k^5 - 2k\bar{a}_k^1 - \bar{a}_k^3 \\ - 2M \left(\hat{D}_{k-1}^1 a_{k-1}^1 + \hat{D}_{k-1}^3 a_{k-1}^3 + a_{k-1}^5 + \hat{E}_{k-1}^1 \bar{a}_{k-1}^1 - 2\bar{a}_{k-1}^3 \right) \\ + 4M^2 \left(\hat{F}_{k-2}^3 a_{k-2}^3 - \bar{a}_{k-2}^3 \right), \quad (\text{A41})$$

$$\hat{C}_k^1 \bar{a}_k^1 = (k+1)\bar{a}_k^3 + \bar{a}_k^5 - 2M \left(\hat{D}_{k-1}^1 \bar{a}_{k-1}^1 + \hat{D}_{k-1}^3 \bar{a}_{k-1}^3 + \bar{a}_{k-1}^5 \right) \\ + 4M^2 \hat{F}_{k-2}^3 \bar{a}_{k-2}^3, \quad (\text{A42})$$

where

$$\hat{C}_k^1 = L+1-k^2, \quad \hat{D}_k^1 = k(k-1), \quad \hat{D}_k^3 = 2(k+1), \\ \hat{E}_k^1 = 1-2k, \quad \hat{F}_k^3 = k+1,$$

$$\hat{C}_k^1 a_k^3 = (k+1)a_k^1 - a_k^5 - \bar{a}_k^1 - 2k\bar{a}_k^3 \\ - 2M \left(\hat{G}_{k-1}^3 a_{k-1}^3 + \hat{G}_{k-1}^1 a_{k-1}^1 + \hat{H}_{k-1}^3 \bar{a}_{k-1}^3 - 2\bar{a}_{k-1}^1 \right) \\ + 4M^2 \left(\hat{I}_{k-2}^3 a_{k-2}^3 + \hat{J}_{k-2}^3 \bar{a}_{k-2}^3 \right), \quad (\text{A43})$$

$$\hat{C}_k^1 \bar{a}_k^3 = (k+1)\bar{a}_k^1 - \bar{a}_k^5 - 2M \left(\hat{G}_{k-1}^3 \bar{a}_{k-1}^3 + \hat{G}_{k-1}^1 \bar{a}_{k-1}^1 \right) \\ + 4M^2 \hat{I}_{k-2}^3 \bar{a}_{k-2}^3, \quad (\text{A44})$$

where

$$\hat{G}_k^3 = 2k^2 - 2 - L, \quad \hat{G}_k^1 = 2k, \quad \hat{H}_k^3 = -4k, \\ \hat{I}_k^3 = k^2 - 1, \quad \hat{J}_k^3 = -2k.$$

$$\hat{C}_k^5 a_k^5 = 2L(a_k^1 - a_k^3) - \hat{D}_k^5 \bar{a}_k^5 + 2M \left(\hat{E}_{k-1}^5 a_{k-1}^5 + 2L a_{k-1}^3 + \hat{D}_{k-1}^5 \bar{a}_{k-1}^5 \right), \quad (\text{A45})$$

$$\hat{C}_k^5 \bar{a}_k^5 = 2L(\bar{a}_k^1 - \bar{a}_k^3) + 2M \left(\hat{E}_{k-1}^5 \bar{a}_{k-1}^5 + 2L \bar{a}_{k-1}^3 \right), \quad (\text{A46})$$

where

$$\hat{C}_k^5 = L + k(1 - k), \quad \hat{D}_k^5 = 2k - 1, \quad \hat{E}_k^5 = k(1 - k) + 2.$$

-
- [1] L. Barack, N. Sago, Phys. Rev. D **81**, 084021 (2010), [arXiv:1002.2386 [gr-qc]].
- [2] J. L. Barton, D. J. Lazar, D. J. Kennefick, G. Khanna, L. M. Burko, Phys. Rev. D **78**, 064042, (2008), [arXiv:0804.1075 [astro-ph]].
- [3] [http://www.ligo.caltech.edu/advLIGO/scripts/summary.shtml].
- [4] [http://www.cascina.virgo.infn.it/advirgo/],
[http://www.cascina.virgo.infn.it/advirgo/docs/whitepaper.pdf].
- [5] [http://lisa.gsfc.nasa.gov/Documentation/LISA-LPF-RP-0001_v1.1.pdf].
- [6] [http://lisa.nasa.gov/].
- [7] F. D. Ryan, Phys. Rev. D **56**, 1845 (1997).
- [8] S. Finn, K. Thorne, Phys. Rev. D **57**, 7089 (1998).
- [9] P. Amaro-Seoane, J. R. Gair, M. Freitag, M.C. Miller, I. Mandel, C. J. Cutler, S. Babak, Class. Quant. Grav. **24**, R113 (2007), [arXiv:astro-ph/0703495].
- [10] L. Barack, C. Cutler, Phys. Rev. D **69**, 082005 (2004), [arXiv:gr-qc/0310125].
- [11] B. S. DeWitt and R. W. Brehme, Annals Phys. **9**, 220 (1960).
- [12] Y. Mino, M. Sasaki and T. Tanaka, Phys. Rev. D **55**, 3457 (1997), [arXiv:gr-qc/9606018].
- [13] T. C. Quinn and R. M. Wald, Phys. Rev. D **56**, 3381 (1997), [arXiv:gr-qc/9610053].
- [14] S. Detweiler and B. F. Whiting, Phys. Rev. D **67**, 024025 (2003), [arXiv:gr-qc/0202086].
- [15] L. Barack and A. Ori, Phys. Rev. D **61**, 061502 (2000), [arXiv:gr-qc/9912010].
- [16] L. Barack, Phys. Rev. D **64**, 084021 (2001), [arXiv:gr-qc/0105040].
- [17] L. Barack, Y. Mino, H. Nakano, A. Ori and M. Sasaki, Phys. Rev. Lett. **88**, 091101 (2002), [arXiv:gr-qc/0111001].
- [18] L. Barack and A. Ori, Phys. Rev. D **67**, 024029 (2003), [arXiv:gr-qc/0209072].
- [19] L. Barack and A. Ori, Phys. Rev. Lett. **90**, 111101 (2003), [arXiv:gr-qc/0212103].
- [20] L. Barack and C. O. Lousto, Phys. Rev. D **72**, 104026 (2005), [arXiv:gr-qc/0510019].
- [21] L. M. Burko, Class. Quant. Grav. **17**, 227 (2000), [arXiv:gr-qc/9911042].
- [22] L. M. Burko and Y. T. Liu, Phys. Rev. D **64**, 024006 (2001), [arXiv:gr-qc/0103008].
- [23] L. Barack and L. M. Burko, Phys. Rev. D **62**, 084040 (2000), [arXiv:gr-qc/0007033].
- [24] L. M. Burko, Phys. Rev. Lett. **84**, 4529 (2000), [arXiv:gr-qc/0003074].
- [25] S. Detweiler, E. Messaritaki and B. F. Whiting, Phys. Rev. D **67**, 104016 (2003), [arXiv:gr-qc/0205079].
- [26] L. M. Diaz-Rivera, E. Messaritaki, B. F. Whiting and S. Detweiler, Phys. Rev. D **70**, 124018 (2004), [arXiv:gr-qc/0410011].
- [27] W. Hikida, S. Jhingan, H. Nakano, N. Sago, M. Sasaki and T. Tanaka, Prog. Theor. Phys. **113**, 283 (2005), [arXiv:gr-qc/0410115].
- [28] R. Haas, Phys. Rev. D **75**, 124011 (2007), [arXiv:gr-qc/0704.0797].
- [29] I. Vega and S. Detweiler, Phys. Rev. D **77**, 084008 (2008), [arXiv:0712.4405].
- [30] L. Barack and C. O. Lousto, Phys. Rev. D **66**, 061502 (2002), [arXiv:gr-qc/0205043].
- [31] T. S. Keidl, J. L. Friedman and A. G. Wiseman, Phys. Rev. D **75**, 124009 (2007), [arXiv:gr-qc/0611072].
- [32] L. Barack and N. Sago, Phys. Rev. D **75**, 064021 (2007), [arXiv:gr-qc/0701069].
- [33] S. Detweiler, E. Poisson, Phys. Rev. D **69**, 084019 (2004), [arXiv:gr-qc/0312010].
- [34] S. Detweiler, Phys. Rev. D **77**, 124026 (2008), [arXiv:0804.3529 [gr-qc]].
- [35] M. V. Berndtson, Ph.D. Dissertation, [arXiv:0904.0033 [gr-qc]].
- [36] N. Sago, L. Barack and S. Detweiler, Phys. Rev. D **78**, 124024 (2008), [arXiv:0810.2530 [gr-qc]].
- [37] E. Poisson, Phys. Rev. D **52**, 5719 (1995); Phys. Rev. D **55**, 7980 (1997).
- [38] N. Warburton, L. Barack (2011), [arXiv:1103.0287 [gr-qc]].
- [39] L. Barack, A. Ori, N. Sago, Phys. Rev. D **78**, 084021 (2008), [arXiv:0808.2315 [gr-qc]].
- [40] E. Poisson, *Living Reviews in Relativity* **7**, 6 (2004).
- [41] L. Barack, Class. Quant. Grav. **26**, 213001 (2009), [arXiv:0908.1664 [gr-qc]].
- [42] T. Regge and J. A. Wheeler, Phys. Rev. **108**, 1063 (1957).
- [43] V. Moncrief, Ann. of Phys. **88**, 323, (1974).
- [44] K. Glampedakis, S. A. Hughes, D. Kennefick, Phys. Rev. D **66**, 044002 (2002), [arXiv:gr-qc/0203086].
- [45] P.C. Peters, J. Matthews, Phys. Rev. **131**, 435 (1963); P. C. Peters, Phys. Rev. **136**, B1224 (1964).
- [46] L. Barack, A. Ori, Phys. Rev. D **64**, 124003 (2001), [arXiv:gr-qc/0107056].
- [47] P. L. Chrzanowski, Phys. Rev. D **11**, 2042 (1975).

- [48] S. Hopper, C. R. Evans, Phys. Rev. D **82**, 084010 (2010), [arXiv.org:1006.4907].
- [49] C. Cutler, D. Kennefick, E. Poisson, Phys. Rev. D **50**, 3816 (1994).
- [50] A. Pound, Phys. Rev. D **81**, 024023, (2010), [arXiv:0907.5107 [gr-qc]].
- [51] E. Rosenthal, Phys. Rev. D **74**, 084018 (2006).
- [52] [http://www.gnu.org/software/gsl/manual/html_node/index.html].
- [53] L. Barack, private communication, 2010.
- [54] S. A. Teukolsky, Astrophys. J. **185**, 635 (1973).
- [55] S. A. Teukolsky and W. H. Press, Astrophys. J. **193**, 443 (1974).